remote sensing

MDPI

Article

Biomass Burning Aerosol Observations and Transport over Northern and Central Argentina: A Case Study

Gabriela Celeste Mulena [1,2,*], Eija Maria Asmi [3], Juan José Ruiz [4], Juan Vicente Pallotta [5] and Yoshitaka Jin [6]

[1] Consejo Nacional de Investigaciones Científicas y Técnicas (CONICET), Ciudad Autónoma de Buenos Aires C1425FQB, Argentina
[2] Servicio Meteorológico Nacional (SMN), Ciudad Autónoma de Buenos Aires C1425GBE, Argentina
[3] Finnish Meteorological Institute (FMI), FI-00101 Helsinki, Finland; eija.asmi@fmi.fi
[4] Centro de Investigaciones del Mar y la Atmósfera (CONICET-Universidad de Buenos Aires), Departamento de Ciencias de la Atmósfera y los Océanos (FCEyN-Universidad de Buenos Aires), Instituto Franco-Argentino para el Estudio del Clima y sus Impactos (IRL IFAECI/CNRS-IRD-CONICET-Universidad de Buenos Aires), Ciudad Autónoma de Buenos Aires C1428EGA, Argentina; jruiz@cima.fcen.uba.ar
[5] Centro de Investigaciones en Láseres y Aplicaciones, UNIDEF (CITEDEF-CONICET), Villa Martelli B1603ALO, Argentina; jpallotta@citedef.gob.ar
[6] National Institute for Environmental Studies (NIES), Tsukuba 305-8506, Japan; jin.yoshitaka@nies.go.jp
* Correspondence: gmulena@smn.gob.ar

Abstract: The characteristics of South American biomass burning (BB) aerosols transported over northern and central Argentina were investigated from July to December 2019. This period was chosen due to the high aerosol optical depth values found in the region and because simultaneously intensive biomass burning took place over the Amazon. More specifically, a combination of remote sensing observations with simulated air parcel back trajectories was used to link the optical and physical properties of three BB aerosol events that affected Pilar Observatory (PO, Argentina, 31°41′S, 63°53′W, 338 m above sea level), with low-level atmospheric circulation patterns and with types of vegetation burned in specific fire regions. The lidar observations at the PO site were used for the first time to characterize the vertical extent and structure of BB aerosol plumes as well as their connection with the planetary boundary layer, and dust particles. Based mainly on the air-parcel trajectories, a local transport regime and a long transport regime were identified. We found that in all the BB aerosol event cases studied in this paper, light-absorbing fine-mode aerosols were detected, resulting mainly from a mixture of aging smoke and dust particles. In the remote transport regime, the main sources of the BB aerosols reaching PO were associated with Amazonian rainforest wildfires. These aerosols were transported into northern and central Argentina within a strong low-level jet circulation. During the local transport regime, the BB aerosols were linked with closer fires related to tropical forests, cropland, grassland, and scrub/shrubland vegetation types in southeastern South America. Moreover, aerosols carried by the remote transport regime were associated with a high aerosol loading and enhanced aging and relatively smaller particle sizes, while aerosols associated with the local transport pattern were consistently less affected by the aging effect and showed larger sizes and low aerosol loading.

Keywords: biomass burning; northern and central Argentina; AERONET; SAVER-Net lidar; HYSPLIT

Citation: Mulena, G.C.; Asmi, E.M.; Ruiz, J.J.; Pallotta, J.V.; Jin, Y. Biomass Burning Aerosol Observations and Transport over Northern and Central Argentina: A Case Study. *Remote Sens.* **2024**, *16*, 1780. https://doi.org/10.3390/rs16101780

Academic Editor: Carmine Serio

Received: 14 March 2024
Revised: 7 May 2024
Accepted: 13 May 2024
Published: 17 May 2024

1. Introduction

Biomass burning (BB) emissions cause severe air pollution, visibility reduction, and public health risks [1,2]. BB emits large amounts of various aerosols and gases and has an important role in the regional and global climate system [3,4]. Aerosols emitted from BB can directly influence Earth's radiative energy balance by the absorbing and scattering of solar radiation [5–7] and indirectly alter the microphysical properties of clouds by acting as cloud condensation nuclei [8,9]. They are composed of various chemical components,

where black carbon and organic carbon are the two most significant ones in terms of light absorption [4].

Large amounts of biomass are burned in South America in mostly human-induced fires related to shifting cultivation, deforestation, and the burning of agricultural wastes—e.g., [10]. Fire activity in the Amazon basin and much of South America coincides with the dry season, from July to December—e.g., [11]. Particularly large fire activity was observed in 2019 during July–December, which affected more than 90.000 km^2 of tropical moist forest biomes, 75% of which were within the Amazonian basin [12].

The northern and central Argentina (NCA, 23°–36°S, 57°–67°W) [13] region is heavily influenced by fire activity during the dry season [11,14]. This region is affected by both local or short-range BB emissions as well as by remote or long-range transport of BB aerosols [11,15]. The long-range tropospheric transport of pollutants is caused by Amazon rainforest wildfires in South America—e.g., [16–19]. These aerosols and gas-phase species are transported to the south by the South American low-level jet (SALLJ), which is a low-level flow with a jet vertical profile whose maximum intensity is below 1.5 km above ground level (AGL) [20]. In addition to the long-range transport of BB pollutants, the short-range transport of BB aerosols towards NCA is controlled by weather regimes associated with mid-latitude synoptic disturbances and the associated transient systems [16]. The origin of these BB aerosols is related to near-range fires, which occur mainly in deforested areas of the tropical forest and temperate cropland, grassland, and scrub/shrubland of territories of southeastern South America (SESA: 20°–36°S, 50°–67°W) (mostly within the Chaco province of Argentina and Paraguay) [11,14]. The Amazonian smoke represents a significant part of the BB-related aerosol loading over the NCA region, explaining between 30 and 40% of the total aerosol loads from August to September [11]. The remaining 60 to 70% of the loads from these months are almost entirely due to SESA fires [11]. Observations show that smoke plumes of BB commonly reach the free troposphere or even exceed it and penetrate the stratosphere [8]. The plume's typical height is defined as an altitude where BB aerosol type is most probably found. In the Amazon region, it can range from a few hundred meters to 6 km AGL; within the planetary boundary layer (PBL), most smoke plumes peak out between 1.6 and 2.5 km AGL—e.g., [21–26].

The characterization of BB aerosol properties usually requires the combination of multiple sources of information, such as circulation models and well-calibrated instrumentation. The lack of direct measurements is one of the issues in researching BB aerosols and how they affect NCA. The Pilar Observatory (PO: 31°41′S, 63°53′W, 338 m above sea level, ASL) is one of the major endeavors in measuring aerosol and gas-phase properties in this region [13].

The wildfires in the region of the Amazonian rainforest in South America have long been identified as one of the largest contributors to BB pollutants globally, with impacts ranging from local to regional and global scales [27]. As a result, the Amazon region has been the focus of several aerosol characterization studies in recent years—e.g., [28–32]. Pérez-Ramírez et al. [33]; Rosário et al. [18]; and Freitas et al. [16], among others, studied aerosol optical properties during the dry season in Amazonia. By contrast, there is a limited number of studies conducted in SESA and NCA because of scarce measurements in these regions. For example, Ulke [34] analyzed the microphysical and optical properties of aerosols and their long-range transport by SALLJ over Buenos Aires city (34°36.2′S, 58°22.9′W, 25 m ASL), located South of the SESA region. Previous studies on aerosols in Argentina have used light detection and ranging (lidar) information from the South American Environmental Risk Management Network (SAVER-Net) to evaluate only the vertical and temporal distribution of aerosol plumes—e.g., [35,36]. Also, the Aerosol Robotic Network (AERONET) sun photometer observation has been used to classify aerosol types from long-term monitoring and to study particular events [13,37]. García et al. [38] and Della Ceca et al. [39] used satellite data and an aerosol transport model to identify sources of aerosol in cities located in the NCA region.

Measurements of aerosol optical depth (AOD), Ängstrom exponent (α), single-scattering albedo (SSA), and fine-mode fraction (FMF) obtained from ground-based or remote sensors can be used to describe the optical properties of aerosols. The AOD is a measure of the extinction of radiation by aerosol scattering and absorption in the atmosphere. This parameter indicates the concentration of aerosol loading present in the atmosphere. High AOD values associated with burning activities were found in South America—e.g., [11]. Notably, Olcese et al. [40] identified short episodes of BB with higher AOD values (up to 0.4) lasting no more than two days at the Centro Espacial Teófilo Tabanera site (31°31′S, 64°2′W, 730 m ASL), situated near the PO site. Most of these episodes have their origin in fires and/or in long-range transport. A similar situation was reported in Buenos Aires by Ulke [15]. The growth of aerosols can be attributed to the process of mass accumulation resulting from the condensation of gaseous sulfuric acid, organic compounds, and other molecules present in the background environment, as well as interactions with other atmospheric contaminants and gases [41]. The α is a measure of the wavelength dependence of AOD and is a qualitative indicator of the dominant particle size. A higher α (>1) can be associated with the prevalence of smaller particles, while a lower α (<1) points to larger particles [41]. The smaller particles are referred to as the fine-mode or accumulation-mode aerosols. These particles have radii between 0.1 and 0.25 μm and are formed due to gas-to-particle conversions mainly from anthropogenic activities. The larger particles comprise the coarse mode. They have radii between 1.0 and 2.5 μm, originating from natural sources such as wind-blown mineral dust and sea salt. Values of α between 1.2 and 2.6 related to BB aerosols have been reported in different parts of South America [35,42,43]. The chemical composition of aerosols changes during their life cycle; this process is referred to as aging effects. In general, the values of α between ~0.8 and 1.5 may be linked to aged BB aerosol plumes—e.g., [44,45]. By contrast, higher α (1.8 or greater) may point to freshly nucleated secondary aerosols and/or younger BB aerosol plumes. These last are mostly made of carbonaceous material, mostly black carbon, and organic carbon, which come from incompletely burned biomass [44,46]. According to Reid et al. [46], aerosol particles age during the course of one to four days, increasing in size on average. The development of particles in the fine mode, which achieves characteristic radii of roughly 0.2 μm, was demonstrated to be explained by mechanisms related to condensation and coagulation [47]. Additionally, aerosols can scatter or absorb shortwave light, as measured by SSA depending on their compositions, shapes, and sizes. SSA is defined as the ratio of aerosol scattering to aerosol extinction, and thus higher values of SSA indicate aerosols that are more highly scattering than absorbing, while lower SSA indicates higher absorbing aerosols. In particular, SSA equal to 1 indicates totally scattering aerosol, and SSA equal to 0 indicates totally absorbing aerosol. In general, BB aerosols originating from forest fires have a higher scattering efficiency and larger particle sizes than those originating from crop, grass, and shrubland fires, which is likely due to the relative contribution difference between flaming and smoldering combustion phases [47,48]. The FMF provides quantitative information on the nature of the size distribution of aerosol particles in the atmosphere. FMF ranges from 0 to 1; when FMF is equal to 1, it represents pure accumulation-mode particles, whereas an FMF equal to 0 represents single coarse-mode particles. Any intermediate FMF value represents a bimodal particle size distribution, where both accumulation and coarse modes can contribute to the total AOD in proportion. Atmospheric aerosols generally have a bimodal particle size distribution.

The combination of AOD and α parameters can help to identify aerosol types based on frequency distributions of AOD and aerosol size distribution—e.g., [42]. The threshold values based on AOD and α for aerosol-type classification depend on particular characteristics of the site of study [35,37]. On average, for specific BB aerosol events, studies over South America reported AOD and α values from AERONET greater than 0.2 and 1, respectively [42,43]. Particularly, in Tucumán city, located in the NCA region, Casasola et al. [37] identified BB aerosol type using AOD at 440 nm greater and equal to 0.2 and α at 440–870 nm between 1.5 and 2.6.

One of the main challenges associated with studying BB aerosols over the NCA region is linking the atmospheric transport mechanisms and type of vegetation burned in fire regions with their optical and physical properties in a data-scarce area.

This study addressed this research challenge by focusing on the characterization of South American BB aerosol smoke plumes transported over the NCA region from July to December 2019. This particular case was selected due to the extreme AOD values detected in the region and because it happened within a period of extreme biomass burning events all over the Amazon [12]. More specifically, we studied the relationship between the aerosol optical and physical properties of selected BB aerosol events at the PO site, atmospheric transport mechanisms, and the vegetation types burned in fire regions (SESA and Amazonia). As a novelty of this study, the information from various sources, including modeling and new remote sensing datasets, was analyzed together. For the first time in the NCA region, the vertical structure and extension of BB aerosol plumes at the PO site, as well as their connection with PBL and the dust particles present in the atmosphere, were studied using ground-based lidar measurements. In this context, new information on the particle extinction coefficients for dust and BB aerosols retrieved from elastic lidar signals was also presented. We also assessed how the height of the air masses controlled by identified atmospheric transport mechanisms changed as they traveled to the PO location.

2. Study Area

In our study, three BB origin regions were defined over South America. These were the Amazonia region (4–20°S, 50–70°W), the SESA region (20–36°S, 50–67°W), and the NCA region (23–35°S, 57–67°W), which is part of the SESA area. The PO site, which belongs to the observation network of the National Meteorological Service of Argentina, was the focus of this study. The location of BB origin regions and the PO site along with the land use and land cover (LULC) classification derived from European Space Agency (ESA) Sentinel-2 imagery [49] is shown in Figure 1. The most common LULC categories in the selected three regions were trees, crops, grasses, and scrubs/shrubs. In SESA, the category "trees" mostly describes the tropical forests, whereas in Amazonia, the prevalent tree type is the rainforest.

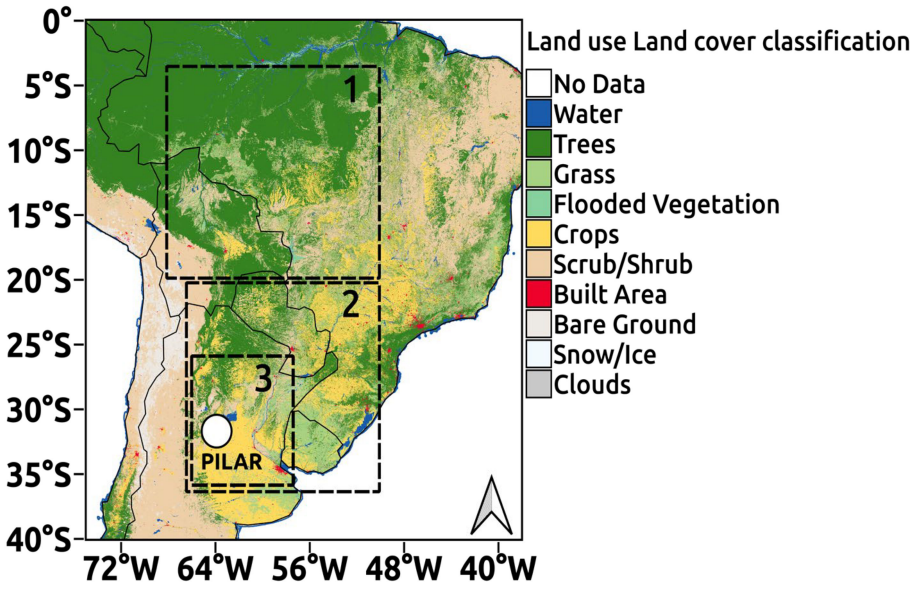

Figure 1. LULC classification over the study area from ESA Sentinel-2 imagery at 10 m resolution (shaded). The white dot indicates the location of Pilar Observatory (31°41′S, 63°53′W, 338 m ASL), while the black squares indicate the location of the Amazonia region (1), the southeastern South America (SESA) region (2), and the northern and central Argentina (NCA) region (3).

3. Materials and Methods

In this study, both observational and numerical modeling data were used. More specifically, the data sources involved in this research were the following: (a) the sun photometer data from AERONET; (b) the multiwavelength Raman and polarization lidar data from SAVER-Net; (c) the carbon monoxide (CO) total column Level 2 data from the TROPOspheric Monitoring Instrument (TROPOMI); (d) the Fire Information for Resource Management System (FIRMS) data from the Moderate Resolution Imaging Spectroradiometer (MODIS); (e) the LULC data from ESA Sentinel-2; and (f) the HYbrid Single-Particle Lagrangian Integrated Trajectory (HYSPLIT) model. Additionally, data from the Cloud–Aerosol Lidar with Orthogonal Polarization (CALIOP) Lidar Level 2 Vertical Feature Mask (VFM) and MODIS True Color were used.

Data and methods used for analysis are described in the following subsections.

3.1. Data

3.1.1. Ground-Based Remote Sensing Measurements

AERONET

The AERONET program is an international federation of standardized ground-based Cimel sun and sky scanning radiometer networks, which includes hundreds of sun photometers covering a large portion of Earth's surface to provide measurements for aerosol research. The program is supported by the National Aeronautics and Space Administration (NASA) and expanded by federation with many non-NASA institutions.

The AERONET sun photometers are set up to measure every 15 min to retrieve AOD at multiple wavelengths (from 340 to 1640 nm) in the whole atmospheric column. These data are utilized to calculate further aerosol optical and physical properties (e.g., volume size distribution, complex index of refraction, among others), provided by the AERONET algorithm [42,50–52]. Further descriptions of the instrumentation, calibration, methodology, data processing, and data quality are described at the AERONET website: https://aeronet.gsfc.nasa.gov/, last access: 25 April 2024.

The PO AERONET site has been active since April 2017, thus providing the longest available dataset in the NCA region. In the current study, we characterized the aerosol optical properties at the PO site with AERONET data Version 3. To ensure the highest quality of data for this study, AERONET Version 3 retrievals at Level 2.0 have been used for AOD, α, and FMF. For the SSA retrievals, AERONET Level 1.5 was used. Because of the strict AERONET Level 2.0 criteria, SSA information is almost always unavailable during the study period at the PO site. So, caution is advised regarding the conclusions derived from SSA in this paper. A similar approach in the NCA region was carried out by Olcese et al. [40].

More specifically, in this study, we calculated the daily and hourly mean values of AOD at 440 nm ($AOD_{(440nm)}$), of α at 440–870 nm ($\alpha_{(440–870nm)}$), of SSA at 440 nm ($SSA_{(440nm)}$), and of FMF of AOD 500 nm ($FMF_{(500nm)}$).

Since the data at the smaller wavelengths are particularly sensitive to BB aerosols, the 440 nm and 500 nm spectral channels and the 440–870 spectral range have been widely used for BB aerosol fraction and optical properties studies in different regions of the planet—e.g., [40,42,43,53]. In this direction, for example, previous studies carried out in the NCA region have reported that the $AOD_{(440nm)}$ and $\alpha_{(440–870nm)}$ relationship shows an optimal separation among different aerosol-type clusters [35,37]. In addition to that, $SSA_{(440nm)}$ and $FMF_{(500nm)}$ have been used in this region to study the absorbing properties and dominant particle size distribution characteristics—e.g., [40]. Level 2.0 hourly data were completed with AERONET 1.5 or 1.0 (if Level 1.5 information was not available) for specific case studies. The Level 1.0 data were carefully quality controlled manually using meteorological and lidar observations, verifying the absence of clouds.

SAVER-Net Network

The SAVER-Net network was developed in the framework of a tri-national project involving Argentina, Chile, and Japan to monitor atmospheric environmental risks such as atmospheric aerosols, stratospheric ozone, and ultraviolet radiation, and to provide real-time information for atmospheric hazards and risk management purposes [54]. For more information, visit: http://www.savernet-satreps.org/es/, last access: 25 April 2024.

The PO SAVER-Net site instrumentation includes a multiwavelength Raman and polarization lidar, which retrieves the optical and physical properties of the atmospheric aerosols.

The PO lidar has been working since April 2017 and is co-located with the AERONET sun photometer described above. The lidar instrument consists of an Nd:YAG laser source emitting at 355, 532, and 1064 nm at 10 Hz with a pulse width between 4 and 7 ns. Its reception system is capable of detecting the elastic lines and three Raman channels: 387, 408, and 607 nm [55]. Each lidar signal is saved with a 10 s acquisition time. After 18 signals are acquired, a 12-minute rest period is taken to extend the laser's flash lamp replacement period.

In this work, the backscatter signal at 1064 nm and two components of the lidar extinction coefficient at 532 nm were used. The first data was used to estimate the heights of BB aerosol plumes. The second information was used to evaluate the physical characteristics of aerosol present in the atmosphere. The lidar extinction coefficient was retrieved from elastic lidar signals using the Fernald inversion method [56], by assuming an extinction-to-backscatter ratio of 50 sr. Next, it was separated into two components (spherical BB aerosol and non-spherical dust aerosols) using depolarization ratio measurement. The separation method is based on the Asian dust and aerosol lidar network (AD-Net) method, which divides aerosol components into spherical (mainly air pollution aerosols) and non-spherical (dust) aerosols [57].

CO Total Column from TROPOMI Instrument

TROPOMI is the single payload aboard the ESA Sentinel-5 Precursor mission, launched in October 2017 [58]. The level of air pollution at the PO site was evaluated using total column CO mass with daily global coverage and a spatial resolution of up to 5.5~7 km^2.

FIRMS and True Color from MODIS Instrument

The product FIRMS uses observations from the MODIS instrument aboard the NASA's Terra and Aqua satellites to detect active fires. The FIRMS product has a spatial resolution of 1 km and a temporal resolution of one day. For more information see https://modis-fire.umd.edu/files/MODIS_C6_Fire_User_Guide_C.pdf, last access: 5 February 2023. The FIRMS algorithm includes a quantification of the fire detection confidence ranging from 0 to 100%. Usually, detections with a confidence level over 30% are considered true detections [59]. In this paper, the analysis of the location of active fires was based on FIRMS/MODIS products. Additionally, this study used True Color images created by the combination of band 1 (645 nm), band 4 (550 nm), and band 3 (470 nm) data of MODIS Level 1B to associate the smoke plumes with fire locations.

LULC Map Derived from ESA Sentinel-2 Satellite

The global map of LULC derived from ESA Sentinel-2 imagery provides ten LULC class types. It is produced at 10 m resolution by a deep learning model trained using over 5 billion hand-labeled Sentinel-2 pixels, sampled from over 20,000 sites distributed across all major biomes in the world [49]. The LULC data were used to determine the vegetation types present in the burned areas.

VFM from CALIOP Instrument

The Cloud–Aerosol Lidar and Infrared Pathfinder Satellite Observations (CALIPSO) satellite was launched by NASA in April 2006 to study the Earth's atmosphere and the impact of clouds and aerosols on climate [60]. This satellite carries the CALIOP instru-

ment, which uses a laser to measure the vertical distribution of clouds and aerosols in the atmosphere. Further information is available on the website: https://calipso.cnes.fr/en/CALIPSO/lidar.htm, last access: 5 February 2023.

In this article, we utilized the CALIPSO lidar Level 2 VFM product. With a horizontal resolution of 333 m and a vertical resolution of 30 m from the ground up to 8.2 km, this product offers information on the altitude and type of atmospheric clouds and aerosols. Aerosol layers in the troposphere are divided into six aerosol subtypes by the CALIPSO aerosol-type identification algorithm. The marine subtype primarily consists of sea salt (i.e., NaCl). The desert dust subtype is mostly associated with mineral soil dust. The clean continental subtype corresponds to background or rural aerosols, which are light-loaded aerosols such as sulfate (SO_4^{2-}), nitrates (NO_3^-), ammonium (NH_4^+), and organic carbon. The polluted continental/smoke subtypes are background aerosols with a substantial fraction of urban pollution and/or a smoke layer with tops lower than 2.5 km AGL. The polluted dust subtype is a mixture of desert dust and smoke or urban pollution. The elevated smoke subtype refers to aged smoke layers that mainly include soot and organic carbon with tops higher than 2.5 km AGL.

3.1.2. HYSPLIT Model

The HYSPLIT Lagrangian trajectory model was developed by the Air Resources Laboratory of the National Oceanic and Atmospheric Administration. The model is a complete system for computing atmospheric trajectories, complex dispersion, and simulations using either puff or Lagrangian particles [61,62]. It is widely used for a variety of applications, such as modeling smoke from wildfires, tracing the source of radionuclides, and modeling volcanic ash dispersion. The model has the capability to combine both Lagrangian and Eulerian approaches to simulate the dispersion of a given substance along the flow. Equations for the calculation of trajectories in HYSPLIT can be found in Stein et al. [63] and references therein. Additional details are available at https://www.ready.noaa.gov/HYSPLIT.php; latest accessed on 5 February 2023.

In this work, we used only the Lagrangian computation of air-parcel trajectories in HYSPLIT model version 4.0 to identify possible source regions for the BB aerosols detected at the PO site during BB aerosol events. Air parcels at the PO site were backtracked up to 72 h prior to their arrival time at the site. These trajectories are computed taking into account the three-dimensional atmospheric flow, but without explicitly considering the potential effect of small-scale or unresolved turbulent effects. Atmospheric flow data with a 1-degree horizontal and 3 h resolution, used in the computation of the back trajectories, are obtained from the Global Data Assimilation System (GDAS). Given the relatively coarse resolution of this dataset, the potential effects of phenomena such as deep convection are not explicitly taken into account in the computation of the trajectories. For more information about the GDAS data visit: https://www.emc.ncep.noaa.gov/gmb/gdas/; latest accessed on 5 February 2023.

Due to possible errors in the numerical methods and input meteorological fields, there are several uncertainties in the trajectory calculation. Therefore, the HYSPLIT was run in ensemble mode, which generates numerous trajectories, to represent the uncertainty related to the computation of the air mass's origin [62]. Each member of the trajectory ensemble shares the same arrival height and starting point, which is the PO site. A fixed grid factor—one meteorological grid point in the horizontal direction and 0.01 sigma units in the vertical—was used to offset the meteorological data to calculate each ensemble member. We employed 27 ensemble members in this work, and we assumed that each member had the same probability of representing the true air mass trajectory.

In this paper, the synoptic-scale circulations associated with BB aerosol intrusions at the PO site were characterized using the GDAS Final Analysis (FNL) with a spatial resolution of 0.25° and a temporal resolution of 6 h. The GDAS/FNL information is available at https://rda.ucar.edu/datasets/ds083.3/index.htmlajax/#description; latest accessed on 25 April 2024.

3.2. Methods

The following method describes the procedures implemented to characterize various aspects of the July–December 2019 BB aerosol events, including the aerosols' optical and physical properties, the atmospheric circulation patterns, and the types of vegetation that were present in the burned areas. The schematic flowchart of methods is shown in Figure 2.

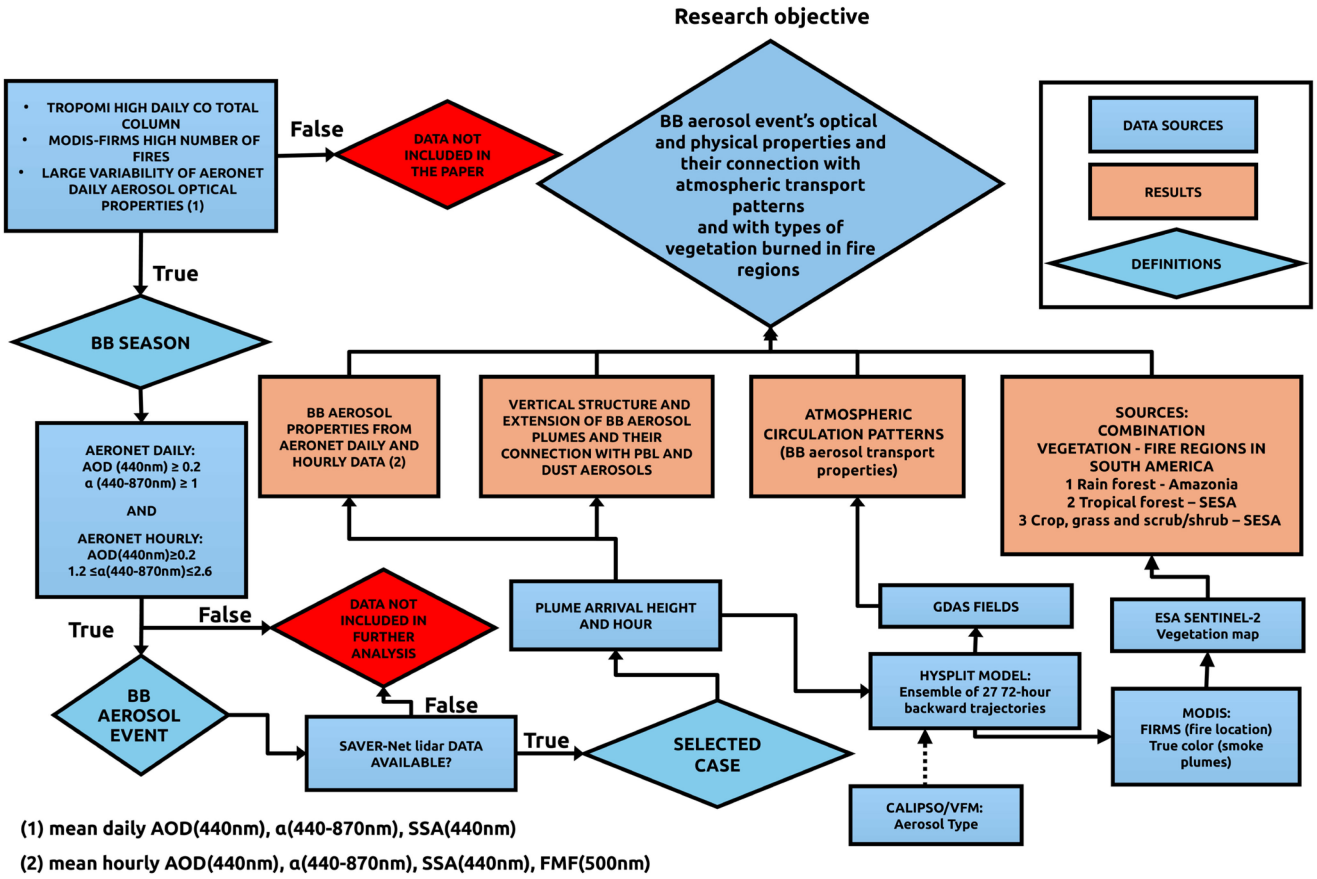

Figure 2. Schematic diagram of the methods used to accomplish the objective of the paper.

For this purpose, we described the monthly and regional distribution of fires for SESA, NCA, and Amazonia using MODIS-FIRMS as well as the daily properties of aerosols at the PO site. These properties of aerosols included the TROPOMI daily CO total column mass, and the mean daily $AOD_{(440nm)}$, $SSA_{(440nm)}$, $\alpha_{(440–870nm)}$, and $FMF_{(500nm)}$ from AERONET. This analysis determined a BB season in the NCA region defined by the peak fire months with high daily CO total column and large variability in aerosol optical properties during the study period.

After this, we defined a BB aerosol event based on AERONET data as those days in which two criteria simultaneously met: mean daily $AOD_{(440nm)} \geq 0.2$ and $\alpha_{(440–870nm)} \geq 1$; with mean hourly $AOD_{(440nm)} \geq 0.2$ and $1.2 \leq \alpha_{(440–870nm)} \leq 2.6$. It was not straightforward to determine the optimal thresholds of $AOD_{(440nm)}$ and $\alpha_{(440–870nm)}$ that best identified the BB aerosol types. The initial thresholds were established from the existing bibliography [37,42,43] and slightly modified to fit our dataset. Our selected two-tiered validation approach, based on daily and hourly timescales, allowed the hourly analysis of BB aerosol events and helped ensure that possible episodes were not excluded from the database. The BB aerosol event where lidar information was available at the PO site was selected for further analysis.

Next, a detailed procedure used to characterize all selected BB aerosol events (i.e., with lidar data available) for this study using multi-source data is outlined.

We investigated the height and hour of their atmospheric BB aerosols arriving at the PO site employing the SAVER-Net lidar and hourly AERONET data. Using this information, we computed the ensemble of 27, 72-h HYSPLIT backward trajectories. The back trajectories were initialized during the BB aerosol event at the PO site, every hour if the mean hourly condition previously mentioned above (mean hourly $AOD_{(440nm)} \geq 0.2$ and $1.2 \leq \alpha_{(440–870nm)} \leq 2.6$) was satisfied. Each starting height for the trajectories was defined as the height of the maximum backscatter detected in the lidar over the time span of the BB aerosol event.

At this point, we identified the low-level atmospheric circulation patterns connected to the BB aerosols reaching the PO site. For this identification, we used mainly the air parcel trajectories and the fields of 0.25° GDAS/FNL data (wind speed, wind direction, and geopotential height). In this stage, we also assessed how the height of the air masses controlled by identified atmospheric transport mechanisms changed as they traveled to the PO location.

Simultaneously, we studied the temporal evolution of the mean daily and hourly optical properties of aerosol ($AOD_{(440nm)}$, $SSA_{(440nm)}$, $\alpha_{(440–870nm)}$, and $FMF_{(500nm)}$) involved in the BB aerosol event. Also, we described the vertical structure and extension of BB aerosol plumes as well as their connection with PBL and dust particles. In this case, the aerosol extinction coefficients retrieved with the AD-Net method were employed to confirm the existence of the spherical BB aerosols previously detected by both PO AERONET and lidar and to investigate the possible presence of non-spherical dust aerosol during the selected BB aerosol event.

Finally, we combined back trajectories with the MODIS True Color image, the MODIS-FIRMS detected fire points, and the ESA Sentinel-2 vegetation cover to specify the type of vegetation burned in fire regions (SESA and Amazonia). Following the paper of Adam et al. [64], our paper accounts only for those MODIS-FIRMS fires with more than 30% confidence that occurred within a range of 50 km from each of the air mass back trajectories ensemble members. The land cover extracted at the fire's location was then used to characterize the vegetation type associated with the fires, potentially contributing to a particular BB aerosol event at the PO site. Eventually, the BB aerosol event could be associated with wild rainforest fires in Amazonia and/or with fires in the SESA region of tropical forest and a mixture of crop, grass, and scrub/shrub. Additionally, we integrated the back-trajectory analysis with the CALIOP-VFM aerosol classification data whenever the back trajectories coincided with the CALIOP instrument's field of view in both space and time.

The information obtained above related to atmospheric circulation patterns and the type of vegetation burned was linked to mean daily $AOD_{(440nm)}$, $SSA_{(440nm)}$, $\alpha_{(440–870nm)}$, and $FMF_{(500nm)}$ properties and also summarized for all cases.

4. Results

4.1. Characterization of the South American Distribution of Fires and the Daily Properties of Aerosols at the PO Site

Figure 3 presents the number of active MODIS-FIRMS fires within the three selected regions and the TROPOMI CO total column mass at the PO site from July to December 2019. Figure 3a(left) shows that, in most regions, the peak of the fire season spans from August to September; however, fire activity was still relevant in Amazonia during July and October. The spatial distribution of the fire spots (August to October 2019) indicates potential sources of BB aerosols (Figure 3a, right). The number of fires in the SESA region remained constant during August and September, with a large contribution of fires (~30%) from the NCA region. Figure 3b shows CO total column mass at the PO site, which reaches higher values from August to October, and maximum values of more than 0.03 mol/m^2 at the ends of August and September, in close agreement with the distribution of the number of fires. During this period, three BB aerosol events were detected based on the criteria described in Section 3.2. These events correspond to local CO total column mass maxima

for August, September, and October. Two of the three events analyzed last for only 1 day, emphasizing their transient nature, while one event lasts for 7 days. Although BB aerosol types were likely present over 26 days, only 9 days meet the requirement for the availability of lidar data.

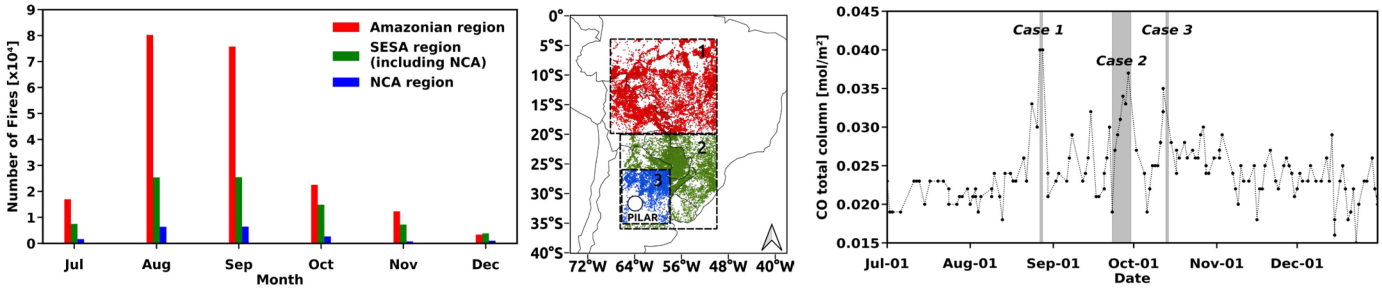

(**a**) (**b**)

Figure 3. (**a**) Number of active fires detected by MODIS-FIRMS in Amazonia (in red), southeastern South America (SESA) (in green), and northern and central Argentina (NCA) (in blue) regions represented in the histogram from July to December 2019 (**left**) and spatial distribution of fire location for the same regions from August to October 2019 (**right**); (**b**) TROPOMI CO total column from July to December 2019 at the Pilar Observatory site. The gray shades indicate the three periods in which BB aerosol event criteria have been met and lidar information was available at the PO site. These three cases are indicated as Case 1, Case 2, and Case 3.

Figure 4 shows the variation of daily averaged $AOD_{(440nm)}$ and $\alpha_{(440–870nm)}$ throughout the study period. The observed mean daily $AOD_{(440nm)}$ was between 0.03 and 0.51, the mean daily $\alpha_{(440–870nm)}$ varied between 0.48 and 1.74, and the mean daily $SSA_{(440nm)}$ fluctuated between 0.6 and 0.99. Overall, the averaged conditions indicated likely a relatively clear atmosphere (mean daily $AOD_{(440nm)} \approx 0.17 \pm 0.09$), with a dominance of fine-mode particles (mean daily $\alpha_{(440–870nm)} \approx 1.17 \pm 0.27$) and a moderate fraction of non-absorbing particles (mean daily $SSA_{(440nm)} \approx 0.9 \pm 0.1$). It is important to note that the average conditions are made considering the gaps in the time series that may arise due to cloudy conditions and/or instrument malfunction.

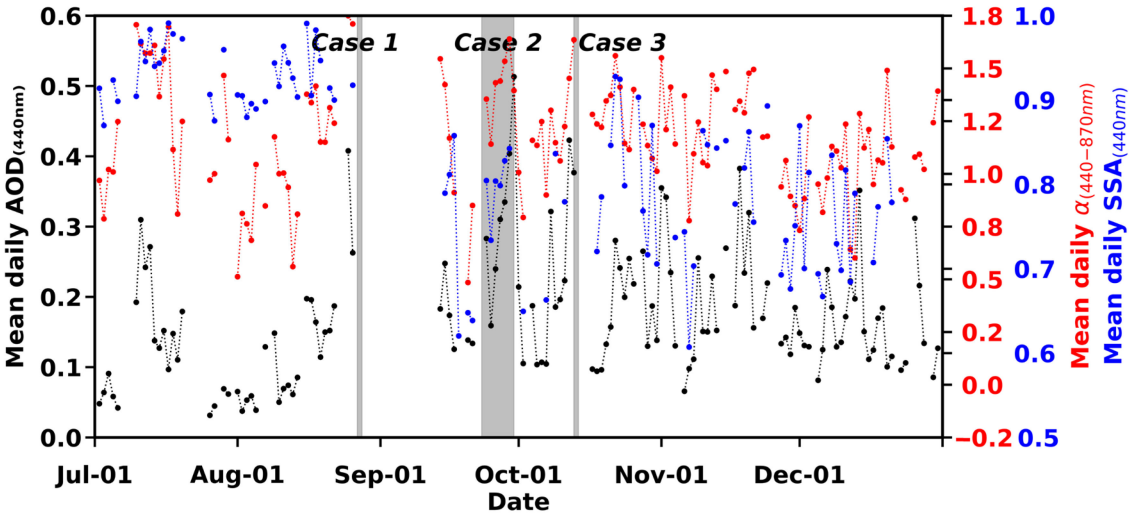

Figure 4. Daily mean $AOD_{(440nm)}$ (black line, left axis), daily mean $\alpha_{(440–870nm)}$ (red line, right axis) by AERONET Level 2.0, and daily mean $SSA_{(440nm)}$ (blue line, right axis) by AERONET Level 1.5 at the Pilar Observatory site from July through December 2019. The gray shades indicate the three periods in which BB aerosol event criteria have been met and lidar information was available at the study site. These three cases are indicated as Case 1, Case 2, and Case 3.

The increase in $AOD_{(440nm)}$ standard deviation during the August–October period is indicative of a large variability in aerosol characteristics, which suggests that the arrival of BB aerosols to PO occurred during sporadic BB aerosol events. This period of August to October 2019 was also characterized by high daily values of the total column CO at the PO site and an elevated number of fire events in South America (Figure 3a(left),b), and, in consequence, can be defined as the BB season of the NCA region. For the BB season, the average daily $SSA_{(440nm)}$ was higher than 0.87, reaching a maximum of 0.93, which suggests the existence of highly scattering particles. Moreover, the daily mean $\alpha_{(440–870nm)}$ covered the range of values found for the study period, indicating the presence of fine- and coarse-mode particles at the site. The minimum and maximum mean daily $AOD_{(440nm)}$ were 0.04 and 0.51 and corresponded to 2 August and 30 September 2019.

Although, in this study, three BB aerosol events have been identified, in the following two subsections, we present a detailed analysis for the 23–30 September 2019 case. The detailed discussion of this case is motivated by its length, intensity, and complexity in terms of the combination of different transport regimes. The properties of the other two cases are briefly discussed in Section 4.4.

4.2. Overall Characteristics of the 23–30 September 2019 BB Aerosol Event

From 23 to 30 September 2019, the PO site recorded the longest-lasting BB aerosol event. Figure 5 shows the time–height distribution of the range-corrected lidar signal at 1064 nm at the PO site. Figures 6 and 7 show the extinction coefficient at 532 nm for BB (spherical) and dust (non-spherical) at the study site. Figure 8 shows the time series of mean hourly $AOD_{(440nm)}$, $SSA_{(440nm)}$, $\alpha_{(440–870nm)}$, and $FMF_{(500nm)}$ and the periods when BB aerosol event criteria were met at the PO site. Figure 9 shows the back trajectories calculated by HYSPLIT for air parcels arriving at the PO site at different arrival times during the BB aerosol event.

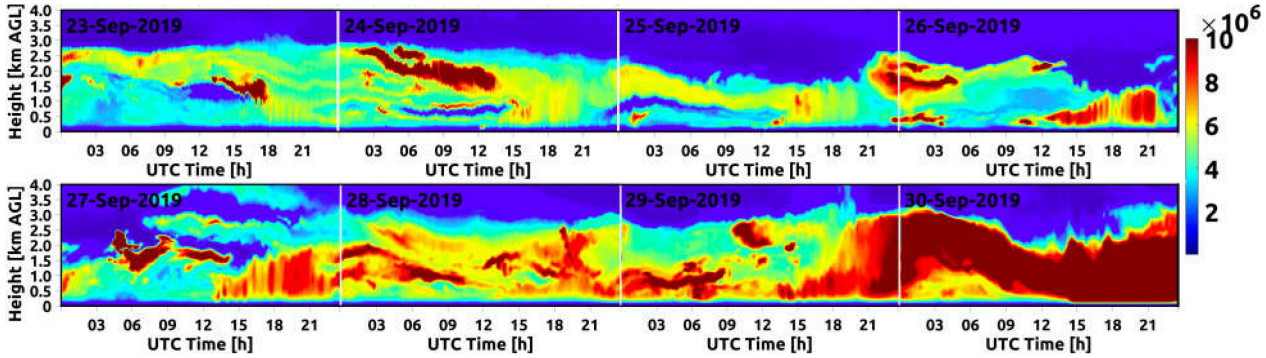

Figure 5. Range-corrected SAVER-Net lidar signal at 1064 nm (arbitrary units) at the Pilar Observatory site from 23 to 30 September 2019.

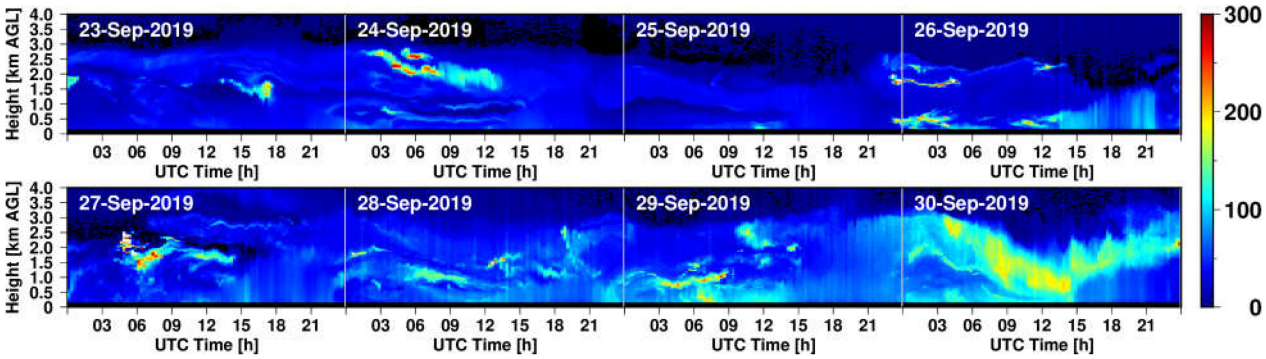

Figure 6. Extinction coefficient at 532 nm (Mm^{-1}) for spherical BB aerosol at Pilar Observatory SAVER-Net lidar from 23 to 30 September 2019.

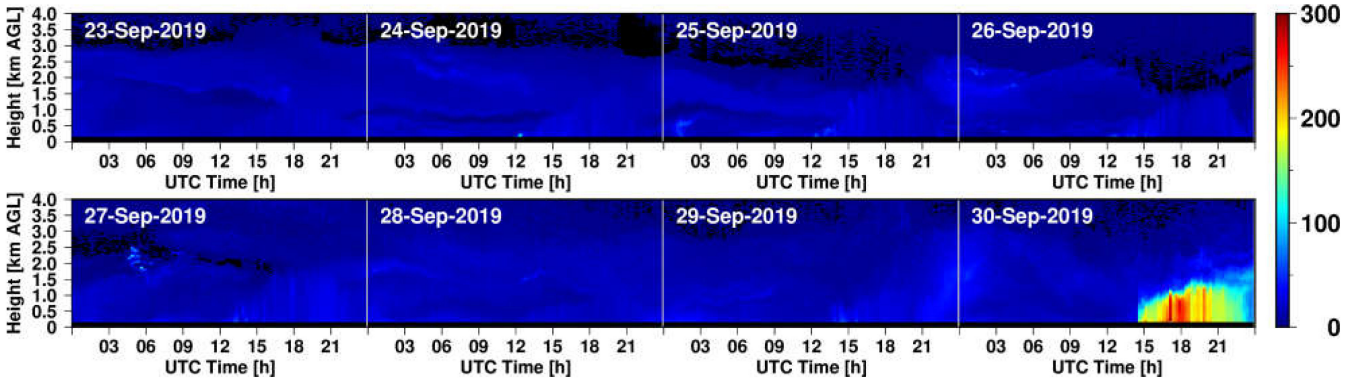

Figure 7. Extinction coefficient at 532 nm (Mm^{-1}) for non-spherical dust aerosol at Pilar Observatory SAVER-Net lidar from 23 to 30 September 2019.

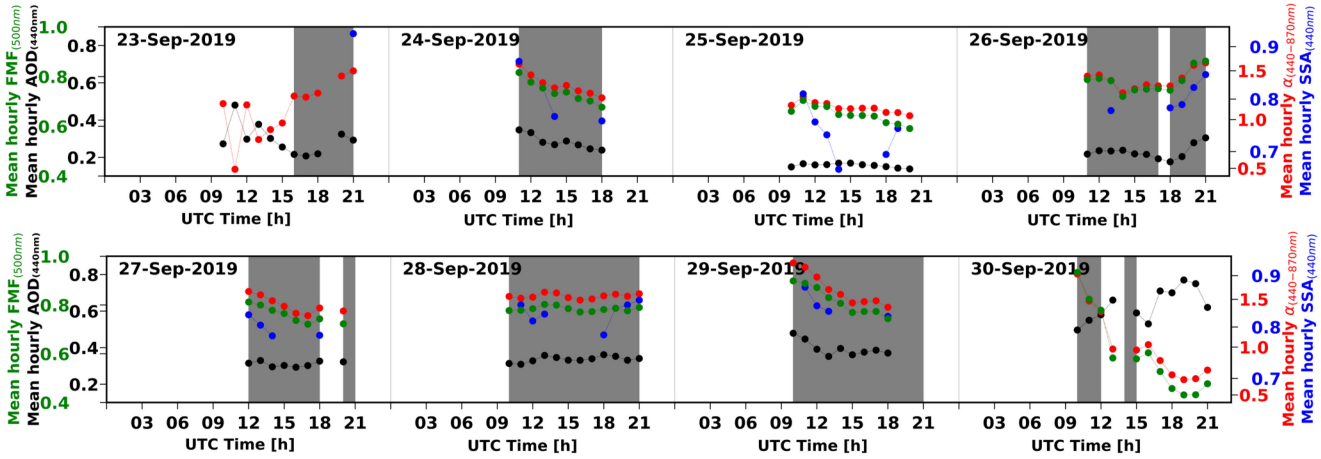

Figure 8. Time series of hourly averages of $AOD_{(440nm)}$ (black line, left axis), $FMF_{(500nm)}$ (green line, left axis), and $\alpha_{(440–870nm)}$ (red line, right axis) by AERONET Level 2.0, and $SSA_{(440nm)}$ (blue line, right axis) by AERONET Level 1.5 at the Pilar Observatory site for 23–30 September 2019. Hourly AERONET Level 1.0 data were used on 23 and 30 September. The gray shade indicates the time span when BB aerosols were found at the site based on hourly AERONET data.

Figure 5 shows two distinct periods in the lidar signal's intensity and structure. A weaker signal period from 23 to 25 September seems to be associated with a plume of aerosols above the surface that is partially mixed with the PBL during the daytime. The growth of the PBL can be well recognized in the lidar data from 23 to 27 September. During these days, a relatively high signal layer started to grow from the surface around 12 UTC (9 a.m. local time). The growth of this layer lasted until the early afternoon, which is consistent with the behavior of a convectively driven PBL. The vertical extent of this layer provides a proxy for the height of the PBL in this period, which roughly reached maximum heights between 1.5 and 2 km AGL. These maximum PBL heights are consistent with the top of the residual layer, subjectively estimated from morning radiosonde data taken at Cordoba airport. During 26–30 September, the lidar signal is much stronger, so it obscures the evolution of the PBL. Figure 8 shows that the mean hourly $AOD_{(440nm)}$, $SSA_{(440nm)}$, $\alpha_{(440–870nm)}$, and $FMF_{(500nm)}$ gradually decreased from 23 to 25 September and increased from 26 to 30 September. This behavior is consistent with the observed intensity of the lidar signals. These two periods are also associated with two particle size distributions: one biased towards larger sizes with light-absorbing properties during the first period, and the other biased towards smaller sizes with less light-absorbing properties during the second period.

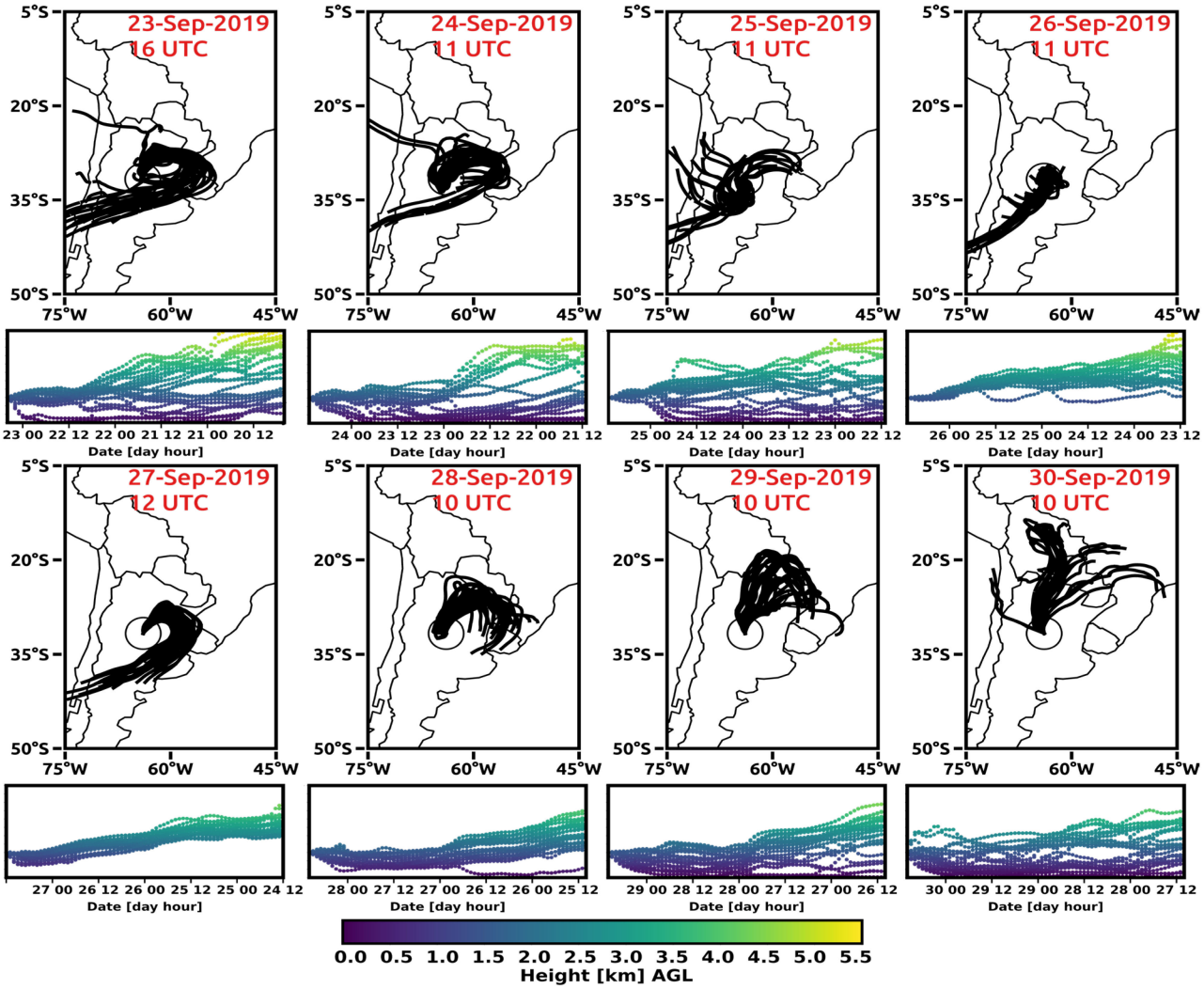

Figure 9. The 27-member ensemble HYSPLIT back trajectories initialized at different hours originating at the Pilar Observatory site at 1.5 km AGL, driven by the 1° GDAS data from the period of 23–30 September 2019. The white dot indicates the location of the Pilar Observatory site.

The results of the extinction coefficients in Figures 6 and 7 show that the lidar signal in Figure 5 consists mostly of BB aerosol plumes. This is in good agreement with the BB aerosol identification results from the AERONET data shown in Figure 8. The maximum extinction coefficient of BB aerosol plumes reaches up to 700 Mm^{-1} at 15:30 UTC on 27 September. Extinction coefficients for dust in Figure 7 show the sudden appearance of dense dust at 15 UTC on 30 September, while the hourly mean values of $\alpha_{(440–870nm)}$ and $FMF_{(500nm)}$ in Figure 8 also indicate the presence of large particles, and the results are consistent with each other. The dust layer height increases with time, reaching an altitude of 1.5 km around 19 UTC. Figure 6 shows that the BB aerosol plume remains above the PBL during this process. The maximum extinction coefficient of dust reaches up to 300 Mm^{-1} at 17 UTC on 30 September.

The upper BB aerosol plume was first detected by lidar above PBL on 23 September (Figure 5). Unfortunately, hourly AERONET Level 2.0 data were not available for this day (Figure 8); however, according to Level 1.0 data, these plumes at 1.5 km AGL may be associated with BB aerosol type starting at 16 UTC (mean hourly $AOD_{(440nm)} \approx 0.21$ and $\alpha_{(440–870nm)} \approx 1.24$). On 24 September, the BB aerosol plume heights gradually descended and mixed into the PBL after 11 UTC. On 25 September, the descending plume with a weak lidar signal was not clearly identified as a BB aerosol event according to our AERONET-based criteria; although, as indicated above, lidar data suggests that this

plume is mainly associated with spherical aerosols. On 26 September, the plume extended upward, reaching a height of 3 km. Compared with previous days, aerosol backscatter intensity increased, and a BB aerosol plume identified by AERONET was merging with the developing PBL starting at 11 UTC. A similar evolution was observed on 27 September. This day, a plume with multiple layers of aerosols was related to BB aerosol type (confirmed by lidar and AERONET daytime observations), and the mean hourly measurements were 0.82 for $SSA_{(440nm)}$, 1.58 for $\alpha_{(440–870nm)}$, 0.31 for $AOD_{(440nm)}$, and 0.81 for $FMF_{(500nm)}$. This plume continued through 28 and 29 September, with a detection of BB aerosols. The lidar image shows that the BB aerosol event peaked on 30 September, which is also reflected by AERONET, especially between 10 and 12 UTC (with hourly mean maximum values of $AOD_{(440nm)} \approx 0.58$, $\alpha_{(440–870nm)} \approx 1.76$, and $FMF_{(500nm)} \approx 0.93$). In summary, for this case, the BB aerosol plume had mean hourly $AOD_{(440nm)}$ values between 0.20 and 0.58, mean hourly $\alpha_{(440–870nm)}$ between 1.22 and 1.88, mean hourly $SSA_{(440nm)}$ from 0.75 to 0.92, and $FMF_{(500nm)}$ from 0.67 to 0.93.

Figure 9 shows that, between 23 and 29 September, most back trajectories originated to the south of PO, reaching the center of SESA, and then went back and reached PO on a north-northeasterly flow. To better understand the resulting trajectories, Figure 10 shows the low-level atmospheric circulation at 850 hPa. During the first part of the event (23–27 September), a weak anticyclonic flow dominated the area surrounding PO. This is the typical circulation found after the passage of cold fronts. A weak north-northeasterly flow is found east of the Andes, which explains the displacement of the air parcels to the south in the last part of the trajectories. A stronger northerly flow from Bolivia to central Argentina started on 28 September, as can be seen in Figure 10. This flow is associated with a SALLJ event. By 30 September, this flow was significantly stronger. The increased SALLJ is directly associated with the highest BB aerosol loading that took place between 10 and 12 UTC on 30 September (Figure 8). After these hours, high $AOD_{(440nm)}$ and lower $\alpha_{(440–870nm)}$ values from hourly AERONET Level 1.0 suggested the presence of dust aerosols. A strong cold front reached the PO site approximately at 15 UTC, producing a sudden increase in the wind speed and a change in the wind direction to the southeast. This change in the low-level circulation is associated with the change in the dominant aerosol type from BB to dust within the PBL, as shown in Figure 6.

Between 23 and 28 September, most trajectories experienced subsidence, some of them starting at altitudes as high as 5.5 km AGL (Figure 9). This behavior is consistent with the weak anticyclonic circulation that dominated the flow during this period (Figure 10). In this event, and due to the subsidence associated with the anticyclonic circulation, the air parcels entered the PBL at the end of their trajectory (i.e., 12–24 h before reaching the PO site). This reduced the time period in which the air parcels were in contact with fire plumes. During 29 and 30 September, the number of trajectories that remain close to the surface for almost the entire track period is significantly higher. This increases the chance for the parcels to interact with fire plumes along the trajectory, particularly those that are far from the PO site.

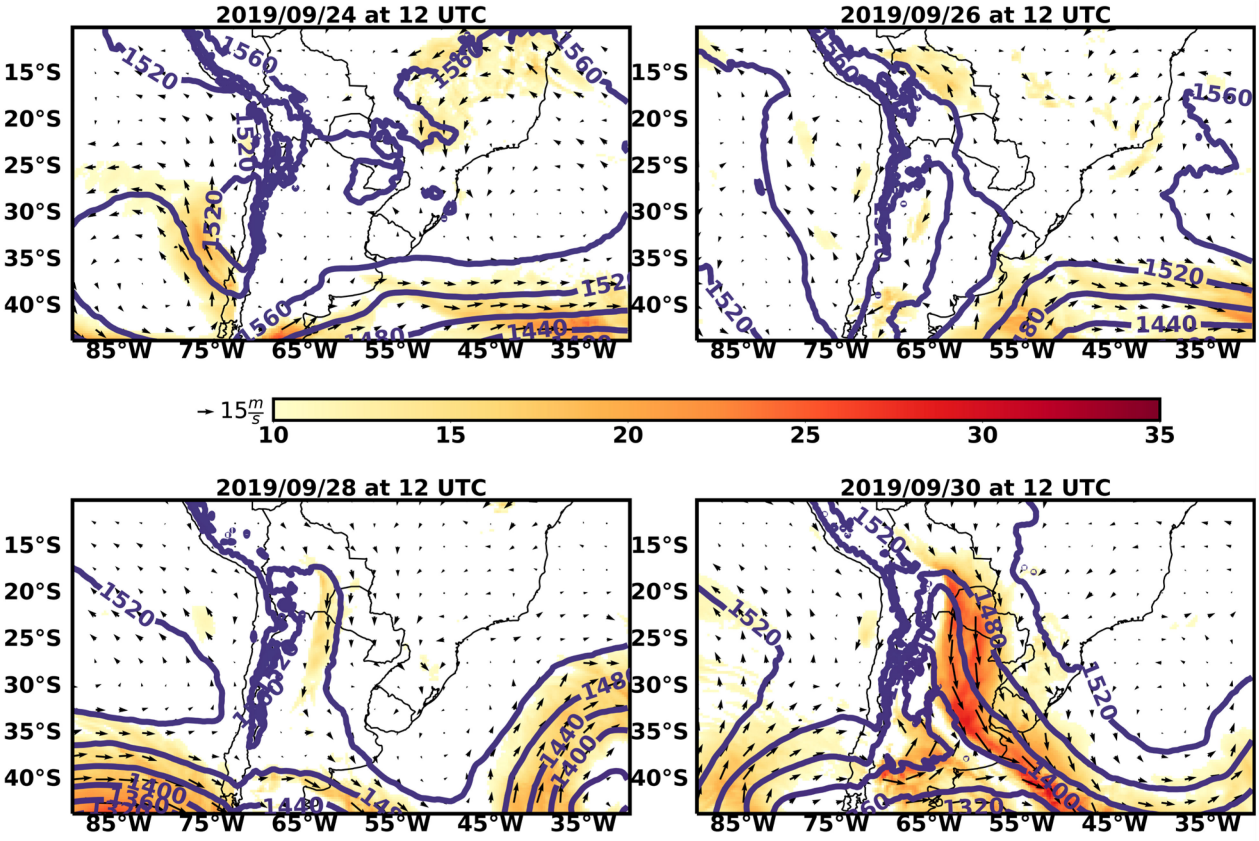

Figure 10. Wind speed (shaded ms−1), wind direction vectors (arrows), and geopotential height (contours, mgp) at 850 hPa for 24 September 2019 at 12 UTC (**upper left**), 26 September 2019 at 12 UTC (**upper right**), 28 September 2019 at 12 UTC (**lower left**), and 30 September 2019 at 12 UTC (**lower right**) from the 0.25° GDAS/FNL analysis.

4.3. Two Case Studies of Short and Long BB Aerosol Transport Events: 27 and 30 September 2019

Figures 11 and 12 depict potential sources for the BB aerosols reaching the PO site along with their possible trajectories on 27 and 30 September 2019.

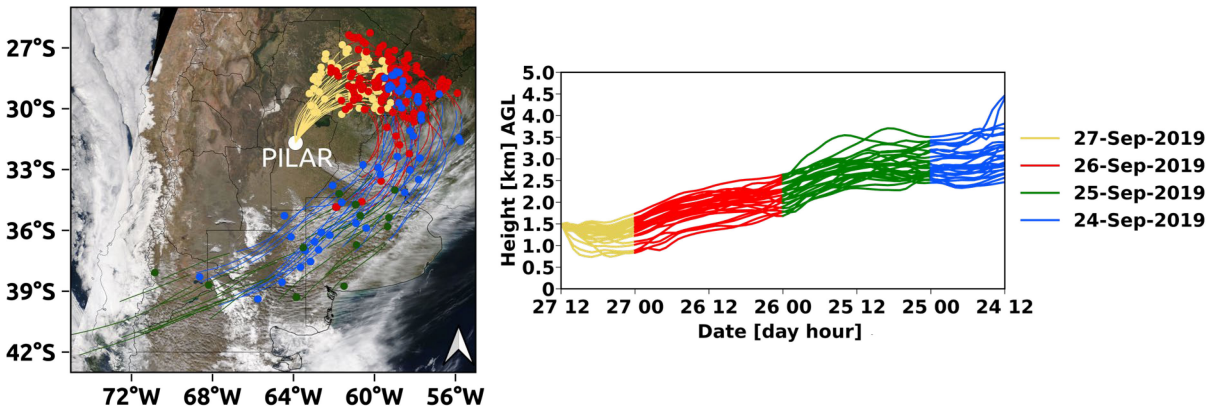

Figure 11. (**left panel**) 72-hour backward trajectories determined with the HYSPLIT model with 27 members starting at the Pilar Observatory site at 1.5 km AGL on 27 September 2019 at 12 UTC. The lines show the air mass back trajectory during 24–27 September. Different colors correspond to different dates, as indicated in the right panel legend. The dots indicate the location of fire points,

and their color indicates the day on which they were within a 50 km range of a back-trajectory ensemble member. The shade corresponds to the True Color image taken by MODIS at 14:05 UTC on 27 September 2019. (**right panel**): Back-trajectory heights as a function of time. Different colors indicate different days, as in the (**left panel**).

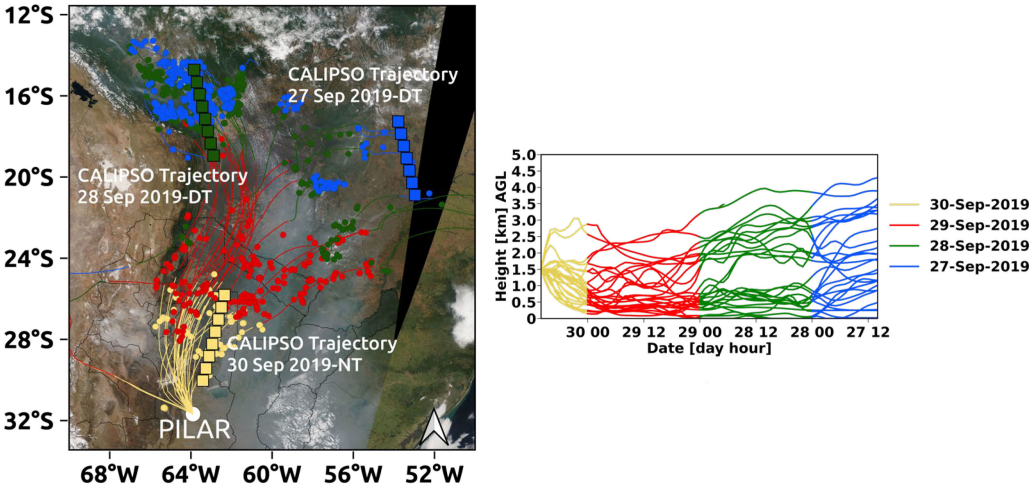

Figure 12. (**left panel**) As in Figure 11, but for 30 September 2019 at 10 UTC. The lines show the air mass back trajectory during 27–30 September. Different colors correspond to different dates, as indicated in the right panel legend. The dots indicate the location of fire points, and their color indicates the day on which they were within a 50 km range of a back-trajectory ensemble member. The shade corresponds to the true color image taken by MODIS at 14:35 UTC on 30 September 2019. The blue, green, and yellow squares in the figure indicate the daytime (DT, ascending) and nighttime (NT, descending) trajectories of the CALIPSO satellite for 27, 28, and 30 September 2019; (**right panel**): Back-trajectory heights as a function of time. Different colors indicate different days, as in the (**left panel**).

Figure 11 shows the results for the 27-member ensemble of HYSPLIT back trajectories initialized on 27 September 2019 at 12 UTC at 1.5 km AGL at the PO site. This figure also shows the superposition of the information of the MODIS True Color image (27 September 2019, 14:05 UTC) and of the MODIS-FIRMS detected fires contained within a range of 50 km of each back-trajectory ensemble member. Back trajectories suggest that the sources of the BB aerosols reaching PO were associated with a short-range transport regime driven by a weak anticyclonic circulation. In general, the height of back trajectories ranged between 1.5 and 4 km AGL. These heights decreased with time, which is consistent with synoptic-scale downward motions associated with the anticyclonic flow. The combination of the MODIS-FIRMS fires and the time–height HYSPLIT back-trajectories data shows that the most likely sources of BB aerosols were located northeast of the SESA region up to one day before reaching PO. At the BB aerosol source region, the fire density reached 60 fires per km^2 and the land cover and land use were dominated by cropland, grassland, and scrub/shrub. At the beginning of the back trajectories, the height of the air parcels was above 2.5 km AGL, which is most likely above the PBL top. Thus, it is unlikely that the fires that were close to the back trajectories during this period contributed to the BB aerosol loading observed at the PO site. The total amount of aerosols produced at the detected fires during this period seems to be relatively low since the MODIS True Color composition did not clearly show smoke plumes associated with the detected fires in northern and central Argentina (and particularly those most likely contributing to BB aerosol loading at the PO site, yellow and red dots in Figure 11).

Figure 12 shows the ensemble of backward trajectories starting at the PO site at 1.5 km AGL on 30 September 2019 at 10 UTC in combination with the MODIS True Color image (30 September 2019, 14:35 UTC) and MODIS-FIRMS fire points. Figure 13 shows the

aerosol sub-type profile from CALIOP-VFM for 27, 28, and 30 September that intersects the back trajectories.

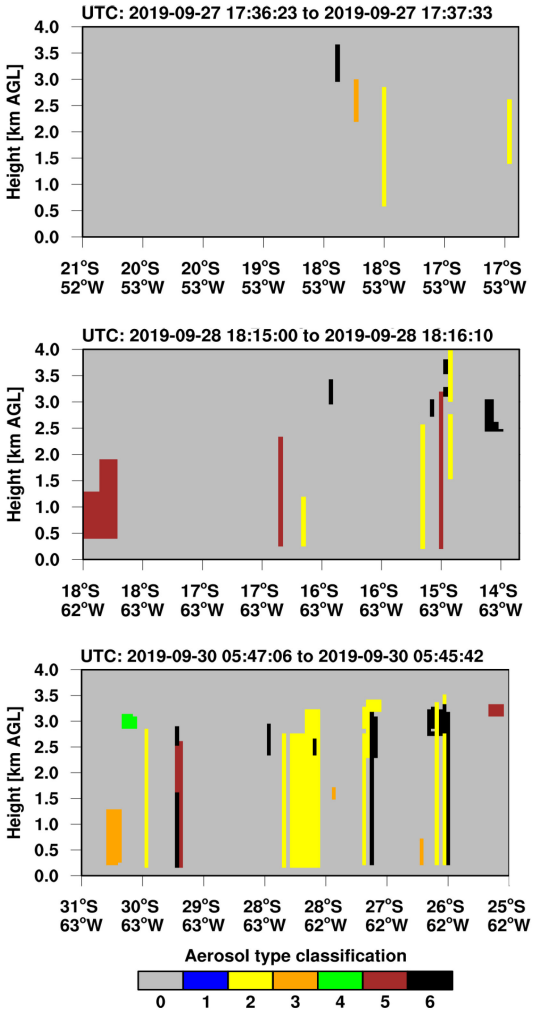

Figure 13. The upper, middle, and lower figures show the aerosol layers measured on the daytime (DT, ascending) and nighttime (DT, descending) trajectories of the CALIOP instrument aboard the CALIPSO satellite for 27, 28, and 30 September 2019. Aerosol types are abbreviated in the legend beneath the image: 0, "Not determined"; 1, "Marine"; 2, "Desert dust"; 3, "Polluted continental/smoke"; 4, "Clean continental"; 5, "Polluted dust"; 6, "Elevated smoke". The images correspond to trajectories identified with blue (**upper panel**), green (**middle panel**), and yellow (**lower panel**) squares in Figure 12.

In this case, the combination of back trajectories and fire points indicated that the most likely sources of the BB aerosols that reached PO were located over the northwestern Amazonia region two days before (Figure 12). The long-range transport or remote regime driven by SALLJ was responsible for carrying these particles to PO. However, some contribution from closer fires over northern Argentina was also possible. The land cover at the fire locations changed along the back trajectories. On 27 and 28 September (long-range transport), the land cover was primarily characterized by rainforests. However, by 30 September (short-range transport), the land cover changes to crop, grass, and scrub/shrub vegetation. Unlike the previous case displayed in Figure 11, most trajectories remained close to the surface during the 72 h prior to arrival at the PO site. This means that air parcels are likely to be within the PBL during most of their displacement, particularly favoring the contribution of long-range aerosol sources from the Amazonia. On this day, a dense smoke plume was revealed by the MODIS True Color image, extending from the Amazonia to the

south up to the NCA region, indicating likely larger total aerosol loads in comparison with the case discussed in Figure 11. The aerosol layer was so thick that it obscured the land from view in several areas.

According to Figure 13, the aerosol subtypes identified by CALIOP-VFM for 27, 28, and 30 September are likely composed mainly by a mixture of dust and smoke aerosols (categories 2, 3, 5, and 6 in Figure 13). Category 2 is related to the "Desert dust" aerosol subtype, which is mostly associated with mineral soil dust. Category 3 is associated with the "Polluted dust" aerosol layer, which is a mixture of desert dust and smoke or urban pollution. Category 5 is linked to the "Polluted continental/smoke" aerosol subtypes, which are background aerosols with a substantial fraction of urban pollution and/or a smoke layer with tops lower than 2.5 km AGL. Category 6 is related to the "Elevated smoke" aerosol subtype, which refers to aged smoke layers that mainly include soot and organic carbon with tops higher than 2.5 km AGL. The particles observed over the study site were probably determined to be a mixture of locally emitted pollutants transported over varying distances. Specifically, the aerosol layers that contributed to the presence of BB aerosols at the PO site on 30 September could be associated with "Elevated smoke" aerosols found in Amazonia on 27 September (upper Figure 13) and 28 (middle Figure 13) and "Polluted continental/smoke" aerosols and "Elevated smoke" aerosols detected in the NCA region on 30 September (lower Figure 13). This description is in close agreement with the identification of an aged BB aerosol plume in Amazonia, transported by the remote pattern into the NCA region previously dominated by layers of fresh smaller particles and of aged larger particles.

4.4. Summary of BB Aerosol Events Characteristics

Table 1 summarizes the properties of the three BB aerosol events detected at the PO site. The table includes values of mean daily $AOD_{(440nm)}$, $SSA_{(440nm)}$, $\alpha_{(440–870nm)}$, and $FMF_{(500nm)}$, obtained from the period of detection of BB aerosol with AERONET data. Different atmospheric transport mechanisms and vegetation types burned at the sources are also identified. Two atmospheric transport mechanisms (local and remote patterns) are observed. The remote pattern is related to the northerly circulation driven by SALLJ. The local pattern is associated with easterly and southerly circulation driven by a weak post-frontal anticyclonic circulation. The types of vegetation burned are mainly rainforest (RF), tropical forest (TF), and a combination of crop, grass, and scrub/shrub (CGSS). RF is mainly located in the Amazonia region, while TF and CGSS predominate in the SESA region.

Table 1 shows that, during the remote transport period, aerosols reaching the PO site originated from fires associated with all the above-mentioned vegetation types. On the other hand, the local pattern carried BB aerosols mainly from the SESA region, which are associated with TF and CGSS vegetation types. It is important to note that BB aerosols from Amazonia may have a higher total aerosol loading contribution than BB aerosols from SESA.

In all three cases, the daily mean values of $\alpha_{(440–870nm)}$ varied from 1.10 to 1.70. The mean daily $SSA_{(440nm)}$ was approximately 0.84. The calculated mean daily $FMF_{(500nm)}$ indicated values in the range from 0.67 to 0.88. The mean daily $AOD_{(440nm)}$ ranged from 0.22 to 0.54. As a result, considering the group of events, the values of these parameters suggested aerosol loading associated with a bimodal particle size distribution biased towards smaller sizes. In consequence, all events were likely dominated by light-absorbing fine-mode aerosols, possibly resulting from a mixture of aging smoke and dust particles.

Observing the longest-lasting BB aerosol event (23–30 September), the mean daily $AOD_{(440nm)}$, $SSA_{(440nm)}$, $\alpha_{(440–870nm)}$, and $FMF_{(500nm)}$ developed from the local to the remote pattern. This implies the existence of two bimodal distributions of particle sizes likely originating from a combination of dust and aged smoke particles: one for the local pattern biased towards larger sizes with light-absorbing properties and lower aerosol loading, and the other for the remote pattern, biased towards smaller sizes with less light-absorbing properties and higher aerosol loading. The enhanced aging of BB aerosols associated

with the remote pattern may be caused by the contribution of BB aerosols from forested areas to the PO site. The scattering efficiency strongly depends on the particle size, and, in consequence, the smaller a particle is, the less efficient the scattering of light that takes place. In this case, the particle density (total number of particles per cm^3) for smaller particle sizes resulting from the remote pattern could probably have increased to compensate for the lower dispersion efficiency. Additionally, we think that the larger particles linked to local patterns may be caused by the transport of fine dust alongside BB aerosols to the site of study.

Table 1. Values of mean daily $AOD_{(440nm)}$, $\alpha_{(440–870nm)}$, and $FMF_{(500nm)}$ by AERONET Level 2.0 and $SSA_{(440nm)}$ by AERONET Level 1.5, and their daily standard deviation (σ) obtained from hourly measurements during the three BB aerosol events (Cases 1, 2, and 3). An asterisk indicates that Level 1.0 hourly AERONET data were used in the computation.

Characteristics	Case 1	Case 2	Case 3
Date	2019-08-26	2019-09-23/24/-/26/27/28/29/30	2019-10-13
Period of detection of BB aerosols UTC Time [h]	11 to 20	16 (09-23) to 12 (09-30)	15 to 20
Transport mechanism	Remote	Local/Local/-/Local/Local/Local/Local/Remote	Local
Mean daily $\alpha_{(440–870nm)}$ (σ)	1.70 (±0.06)	1.10 */1.36/-/1.41 1.43/1.53/1.60/1.54 * (~±0.22)	1.64 (±0.06)
Mean daily $SSA_{(440nm)}$ (σ)	0.91 (±0.02)	0.92/0.80/-/0.80 0.80/0.83/0.84/N/D (~±0.03)	N/D
Mean daily $FMF_{(500nm)}$ (σ)	0.88 (±0.02)	0.67 */0.73/-/0.77 0.76/0.78/0.81/0.84 * (~±0.05)	0.86 (±0.02)
Mean daily $AOD_{(440nm)}$ (σ)	0.25 * (±0.04)	0.3 */0.30/-/0.23 0.32/0.33/0.40/0.54 * (~±0.08)	0.39 (±0.06)
Vegetation type	RF+CGSS	CGSS/CGSS/-/CGSS/CGSS/TF+CGSS/TF+CGSS/TF+RF+CGSS	CGSS

5. Discussion and Conclusions

In this paper, the characteristics of South American biomass burning (BB) aerosols transported over the northern and central Argentina (NCA) region were investigated from July to December 2019. More specifically, we studied the link between the optical and physical properties of three BB aerosol events that affected Pilar Observatory (PO, Argentina, 31°41′S, 63°53′W, 338 m ASL), the atmospheric transport mechanisms, and the vegetation types burned in the identified fire regions. Two patterns of atmospheric circulation—a local pattern and a remote pattern—were examined in the framework of the research. The sources of origin of these BB aerosols were associated with wild rainforest fires in Amazonia and with fires in southeastern South America (SESA) of tropical forest and a mixture of crop, grass, and scrub/shrub. The objective of the paper was achieved by combining data from remote sensing measurements with trajectory modeling. For the first time in the NCA region, the vertical structure and extension of BB aerosol plumes at the PO site as well as their connection with PBL and dust were estimated by ground-based lidar. In this context, the BB and dust particle extinction coefficients retrieved from elastic lidar signals were presented. We also assessed how the height of the air masses driven by the atmospheric transport mechanisms changed as they traveled to the PO site.

We found that the selected BB aerosol events correspond to local maxima in the CO total column mass estimated by TROPOMI during August–October (BB season). The high variability in the mean daily $AOD_{(440nm)}$ for this period suggests that the arrival of BB aerosols at the PO site occurred during sporadic BB aerosol events rather than continuously. These results are consistent with findings reported by Ulke [15] in Buenos Aires city and Olcese et al. [40] at the Centro Espacial Teófilo Tabanera site (situated near the PO site), regarding the sporadic occurrence of the events and, consequently, a relatively low frequency of days with smoke particles annually.

The results indicate that the type of vegetation burned as well as the atmospheric transport patterns can lead to variations in the BB aerosol's optical and physical properties, which were examined both on hourly and daily time scales. Based on the analysis of the three selected BB aerosol event cases, we reach the following conclusions:

The local transport pattern was associated with a northeastern postfrontal anticyclone circulation that carries BB aerosols to the PO site from the SESA region, including the NCA region. The air mass back trajectories that arrived at the PO site, with a prevailing southeasterly or southerly wind direction, typically traveled above 1.5 km AGL. As a result, the only fires that had the potential to contribute effectively to the aerosol loading at PO were those that were close by (less than 2000 km). These fires may involve BB aerosol plumes that can reach at least 1.5 km AGL on average.

The remote pattern was linked with a northerly circulation driven by the South American low-level jet (SALLJ) and which was responsible for transporting BB aerosols to the study site from remote sources in the Amazonia as well as from closer sources within the SESA region. The back trajectories that arrive at the PO site associated with a predominant northerly or northeasterly wind direction tend to travel very close to the surface. This situation would facilitate the long-range transport of the aerosols from Amazonia to the PO site. Our results add to the understanding of the BB aerosol transport routes in South America and confirm the findings from previous studies on the importance of BB for the boundary layer aerosol budgets—e.g., [15–19,21–26].

The values of mean daily $AOD_{(440nm)}$, $\alpha_{(440–870nm)}$, $SSA_{(440nm)}$, and $FMF_{(500nm)}$ suggest a bimodal distribution of aged BB aerosols with light-absorbing properties biased towards smaller sizes when averaged for all three BB aerosol events.

During the longest-lasting BB aerosol event observed in this work, the values of optical and physical parameters followed a gradual change from the local to the remote pattern. Analysis of this event implies that the local pattern contained rather aged, larger-size light-absorbing particles and lower aerosol loadings, while the remote pattern contained aged, smaller-size particles with lower absorption and higher aerosol loadings. These results are consistent with the findings of the smoke particle analysis carried out in the SESA region by previous studies. In this direction, Ulke [15] shows how BB aerosol events, that were observed in Buenos Aires during northerly circulation, showed a statistically significant increase in aerosol optical depth and Ångström exponent, reflected by an increase in the peak of the derived volume size distribution in the fine fraction size range, which also shifts slightly towards bigger radii. Olcese et al. [40] also highlighted that trajectories arriving at the Centro Espacial Teófilo Tabanera site from the Northeast region also lead to a large amount of fine particles, probably having an origin related to biomass burning. We hypothesize that the enhanced aging of BB aerosols associated with the remote pattern may be caused by the contribution of BB aerosols from forested areas to the PO site. In these areas, mainly linked to Amazonia, CALIOP-VFM identified a mixture of dust and smoke aerosols. The reduced scattering efficiency could be compensated by the number concentration of smaller particles during the remote pattern period. Additionally, we acknowledge that the larger particles linked to the local pattern may have a contribution that originated by the transport of fine dust alongside the BB aerosols' trajectory to the PO site. We plan to study in more detail the dust aerosol characteristics and origin over the PO site, during the longest-lasting BB aerosol event.

In the last case of study, lidar showed multiple high-signal layers associated with BB aerosols extending from the surface up to 3 km AGL. Some of these layers were eventually mixed within the convective-driven diurnal PBL. The analysis of the polarized lidar signal at 532 nm enables the separation of BB and dust particle profiles for the days under consideration, revealing the dynamics of these two particle groups. The BB aerosol plumes were detected arriving at the PO site on 23 September and intensified significantly on 30 September, when the maximum intensity of the northerly low-level jet was reached. By the afternoon of 30 September, the BB aerosol plume was mixed within the PBL with dust possibly associated with the wind shift and gustiness produced by a strong cold front. The average height of BB smoke plumes arriving at the PO site in this study was 1.5 km AGL. This is in good agreement with the previous results published in South America—e.g., ~1.5 km [22,24]; ~2 km [21,25]; 2.25 km [23].

The methodology used in this study provides additional insight into aerosol transport mechanisms in the South American region, bringing important information about potential aerosol sources and their characteristics, which can be used for better understanding the potential health impacts of aerosol exposure and developing effective strategies to mitigate the effects of aerosols on air quality. While acknowledging the limitations of the approach based on selected case studies, our results successfully contribute to filling the major gap in the knowledge on aerosols and aerosol transport in the NCA region.

Future research directions should focus on a more accurate characterization of the aerosol properties, so that the aerosol types estimated from remote sensors can be compared against aerosol type estimations based on in situ observations. This is essential to better narrow the potential sources of the aerosols as well as possible modification processes along their transport. Another interesting research avenue for future studies is to conduct a comprehensive characterization of the impact of regional circulation patterns on the aerosol properties within the study area. This can be achieved, for example, by performing back-trajectory analysis over a longer study period and under different fire activity scenarios. Also, more research is required to understand the impact of climate variability at different time scales on aerosol transport as well as the impact of fire activity variability. On the methodological side, future research should focus on incorporating advanced source estimation approaches that incorporate different sources of uncertainty in the computation of the backward trajectories (e.g., uncertainties associated with small-scale turbulence and deep convection, among others), as well as an objective and robust way to link the properties of the sources with those of the detected aerosols.

Author Contributions: Conceptualization, investigation, methodology, data curation, project administration, writing original draft, review, and editing, G.C.M.; conceptualization, investigation, data curation, writing original draft, review, editing, and funding acquisition, E.M.A. and J.J.R.; data curation (lidar), resources, writing—review and editing, J.V.P.; data curation (lidar), resources, formal analysis (lidar), methodology (lidar), Y.J. All authors have read and agreed to the published version of the manuscript.

Funding: This research has also been supported by the National Agency for the Promotion of Science and Technology of Argentina (PICT-2020-SERIEA-01168) and the Academy of Finland ACCC Flagship funding (grant no. 337552), and the Japan Society for the Promotion of Science (JSPS) KAKENHI (grant no. 18KK0289).

Data Availability Statement: The AERONET data can be obtained from https://aeronet.gsfc.nasa.gov/(last access: 25 April 2024). The FIMS data from MODIS can be downloaded from https://firms.modaps.eosdis.nasa.gov/download/ (last access: 5 February 2023). The MODIS True Color images can be obtained from https://worldview.earthdata.nasa.gov/ (last access: 5 February 2023). The CALIPSO lidar Level 2 VFM can be downloaded from https://www-calipso.larc.nasa.gov/tools/data_avail/ (last access: 5 February 2023). To download LULC derived from ESA Sentinel-2 product data visit: https://livingatlas.arcgis.com/landcoverexplorer/#mapCenter=-24.556,-23.094,2&mode=step&timeExtent=2017,2021&year=2022&landCover=Bare+Ground&downloadMode=true (last access: 5 February 2023). The 1° GDAS data are archived at https://www.ready.noaa.gov/data/archives/gdas1/ (last access: 5 February 2023). The 0.25° GDAS/FNL data are available at https:

//rda.ucar.edu/datasets/ds083.3/ (last access: 25 April 2024). The lidar data from SAVER-Net can be requested by the corresponding author.

Acknowledgments: The researchers would like to acknowledge funding received from the National Agency for the Promotion of Science and Technology of Argentina and the Academy of Finland ACCC Flagship funding. The authors thank the support of the National Scientific and Technical Research Council (CONICET), the Finnish Meteorological Institute (FMI), the Research Center for the Sea and the Atmosphere of the University of Buenos Aires (CIMA-UBA, CONICET), the National Meteorological Service of Argentina (SMN), the Center for Research in Lasers and Application (UNIDEF, CITEDEF-CONICET), and the Ministry of Defense of Argentina. The authors would like to thank the lidar operators and the SMN machine shop for their collaboration on the construction and update of the lidar systems and related subsystems, and especially to Elian Wolfram and Sebastian Papandrea. The authors would like to express their sincere gratitude to the Japan International Cooperation Agency (JICA) and Japan Science and Technology Agency (JST) for the financial support of the SAVER-Net project. The authors also thank the AERONET teams, especially to Eduardo Quel, Lidia Otero, and Raul D'Elia. The authors thank the reviewers and editors for all useful and helpful comments on our manuscript.

Conflicts of Interest: The authors declare that they have no known competing financial interests or personal relationships that could have appeared to influence the work reported in this paper.

Abbreviations

The alphabetical list of acronyms used in this paper, along with their expanded form.

AD-Net	Asian dust and aerosol lidar network
AERONET	Aerosol Robotic Network
AGL	Above ground level
AOD	Aerosol optical depth
$AOD_{(440nm)}$	Aerosol optical depth at 440 nm
ASL	Above sea level
BB	Biomass burning
CALIOP	Cloud–Aerosol lidar with Orthogonal Polarization
CALIPSO	Cloud–Aerosol lidar and Infrared Pathfinder Satellite Observations
CGSS	Crop, grass, and scrub/shrub
CO	Carbon monoxide
ESA	European Space Agency
FIRMS	Fire Information for Resource Management System
FMF	Fine-mode fraction
$FMF_{(500nm)}$	Fine-mode fraction of aerosol optical depth at 500 nm
GDAS	Global Data Assimilation System
HYSPLIT	HYbrid Single-Particle Lagrangian Integrated Trajectory
lidar	Light detection and ranging
LULC	Land use and land cover
MODIS	Moderate Resolution Imaging Spectroradiometer
NASA	National Aeronautics and Space Administration
NCA	Northern and central Argentina
PBL	Planetary boundary layer
PO	Pilar Observatory
RF	Rainforest
SALLJ	South American low-level jet
SAVER-Net	South American Environmental Risk Management Network
SESA	Southeastern South America
SSA	Single-scattering albedo
$SSA_{(440nm)}$	Single-scattering albedo at 440 nm
TF	Tropical forest
TROPOMI	TROPOspheric Monitoring Instrument
VFM	Vertical feature mask
α	Ängstrom exponent
$\alpha_{(440–870nm)}$	Ängstrom exponent at 440–870 nm

References

1. Martin, S.T.; Andreae, M.O.; Artaxo, P.; Baumgardner, D.; Chen, Q.; Goldstein, A.H.; Guenther, A.; Heald, C.L.; Mayol-Bracero, O.L.; McMurry, P.H.; et al. Sources and Properties of Amazonian Aerosol Particles. *Rev. Geophys.* **2010**, *48*, RG2002. [CrossRef]
2. World Health Organization. *WHO Global Air Quality Guidelines: Particulate Matter (PM2.5 and PM10), Ozone, Nitrogen Dioxide, Sulfur Dioxide and Carbon Monoxide*; World Health Organization: Geneva, Switzerland, 2021.
3. Forster, P.; Ramaswamy, V.; Artaxo, P.; Berntsen, T.; Betts, R.; Fahey, D.W.; Haywood, J.; Lean, J.; Lowe, D.C.; Myhre, G.; et al. Changes in Atmospheric Constituents and in Radiative Forcing. In *Climate Change 2007: The Physical Science Basis. Contribution of Working Group I to the 4th Assessment Report of the Intergovernmental Panel on Climate Change 2007*; Cambridge University Press: Cambridge, UK, 2007.
4. Arias, P.A.; Bellouin, N.; Coppola, E.; Jones, R.G.; Krinner, G.; Marotzke, J.; Naik, V.; Palmer, M.D.; Plattner, G.-K.; Rogelj, J.; et al. (Eds.) Technical Summary. In *Climate Change 2021: The Physical Science Basis. Contribution of Working Group I to the Sixth Assessment Report of the Intergovernmental Panel on Climate Change*; Cambridge University Press: Cambridge, UK, 2021; pp. 33–144.
5. Ackerman, A.; Toon, O.; Stevens, D.; Heymsfield, A.; Ramanathan, V.; Welton, E. Reduction of Tropical Cloudiness by Soot. *Science* **2000**, *288*, 1042–1047. [CrossRef] [PubMed]
6. Artaxo, P.; Oliveira, P.H.; Lara, L.L.; Pauliquevis, T.M.; Rizzo, L.V.; Junior, C.P.; Paixão, M.A.; Longo, K.M.; Freitas, S.; Correia, A.L. Efeitos Climáticos de Partículas de Aerossóis Biogênicos e Emitidos Em Queimadas Na Amazônia. *Rev. Bras. Meteorol.* **2006**, *21*, 122–168.
7. Procopio, A.S.; Artaxo, P.; Kaufman, Y.J.; Remer, L.A.; Schafer, J.S.; Holben, B.N. Multiyear Analysis of Amazonian Biomass Burning Smoke Radiative Forcing of Climate. *Geophys. Res. Lett.* **2004**, *31*, L03108. [CrossRef]
8. Andreae, M.O.; Rosenfeld, D.; Artaxo, P.; Costa, A.A.; Frank, G.P.; Longo, K.M.; Silva-Dias, M.A.F. Smoking Rain Clouds over the Amazon. *Science* **2004**, *303*, 1337–1342. [CrossRef] [PubMed]
9. Koren, I.; Kaufman, Y.J.; Remer, L.A.; Martins, J.V. Measurement of the Effect of Amazon Smoke on Inhibition of Cloud Formation. *Science* **2004**, *303*, 1342–1345. [CrossRef] [PubMed]
10. Jacobson, M.Z. Effects of Biomass Burning on Climate, Accounting for Heat and Moisture Fluxes, Black and Brown Carbon, and Cloud Absorption Effects. *J. Geophys. Res. Atmos.* **2014**, *119*, 8980–9002. [CrossRef]
11. Videla, F.C.; Barnaba, F.; Angelini, F.; Cremades, P.; Gobbi, G.P. The Relative Role of Amazonian and Non-Amazonian Fires in Building up the Aerosol Optical Depth in South America: A Five Year Study (2005–2009). *Atmos. Res.* **2013**, *122*, 298–309. [CrossRef]
12. Cardil, A.; De-Miguel, S.; Silva, C.A.; Reich, P.B.; Calkin, D.; Brancalion, P.H.S.; Vibrans, A.C.; Gamarra, J.G.P.; Zhou, M.; Pijanowski, B.C.; et al. Recent Deforestation Drove the Spike in Amazonian Fires. *Environ. Res. Lett.* **2020**, *15*, 121003. [CrossRef]
13. Ristori, P.; Otero, L.; Jin, Y.; Barja, B.; Shimizu, A.; Barbero, A.; Salvador, J.; Bali, J.L.; Herrera, M.; Etala, P.; et al. SAVER-Net lidar Network in Southern South America. In Proceedings of the EPJ Web of Conferences, The 28th International Laser Radar Conference (ILRC 28), Bucharest, Romania, 25–30 June 2017; Volume 176, p. 9011. [CrossRef]
14. Puliafito, S.E.; Bolaño-Ortiz, T.; Berná, L.; Flores, R.P. High Resolution Inventory of Atmospheric Emissions from Livestock Production, Agriculture, and Biomass Burning Sectors of Argentina. *Atmos. Environ.* **2020**, *223*, 117248. [CrossRef]
15. Ulke, A.G. Influence of Regional Transport Mechanisms on the Fingerprint of Biomass-Burning Aerosols in Buenos Aires. *Adv. Meteorol.* **2019**, *2019*, 6792161. [CrossRef]
16. Freitas, S.R.; Longo, K.M.; Silva Dias, M.A.F.; Silva Dias, P.L.; Chatfield, R.; Prins, E.; Artaxo, P.; Grell, G.A.; Recuero, F.S. Monitoring the Transport of Biomass Burning Emissions in South America. *Environ. Fluid Mech.* **2005**, *5*, 135–167. [CrossRef]
17. Silva Dias, M.A.F. da Meteorologia, Desmatamento e Queimadas Na Amazônia: Uma Síntese de Resultados No LBA. *Rev. Bras. Meteorol.* **2006**, *21*, 190–199.
18. do Rosário, N.E.; Longo, K.M.; de Freitas, S.R.; Yamasoe, M.A.; Fonseca, R.M. da Modeling the South American Regional Smoke Plume: Aerosol Optical Depth Variability and Surface Shortwave Flux Perturbation. *Atmos. Chem. Phys.* **2013**, *13*, 2923–2938. [CrossRef]
19. de Oliveira, A.M.; Mariano, G.L.; Alonso, M.F.; Mariano, E.V.C. Analysis of Incoming Biomass Burning Aerosol Plumes over Southern Brazil. *Atmos. Sci. Lett.* **2016**, *17*, 577–585. [CrossRef]
20. Vera, C.; Higgins, W.; Amador, J.; Ambrizzi, T.; Garreaud, R.; Gochis, D.; Gutzler, D.; Lettenmaier, D.; Marengo, J.; Mechoso, C.R.; et al. Toward a Unified View of the American Monsoon Systems. *J. Clim.* **2006**, *19*, 4977–5000. [CrossRef]
21. Baars, H.; Ansmann, A.; Althausen, D.; Engelmann, R.; Heese, B.; Müller, D.; Artaxo, P.; Paixao, M.; Pauliquevis, T.; Souza, R. Aerosol Profiling with Lidar in the Amazon Basin during the Wet and Dry Season. *J. Geophys. Res. Atmos.* **2012**, *117*, D21201. [CrossRef]
22. Andreae, M.O.; Artaxo, P.; Beck, V.; Bela, M.; Freitas, S.; Gerbig, C.; Longo, K.; Munger, J.W.; Wiedemann, K.T.; Wofsy, S.C. Carbon Monoxide and Related Trace Gases and Aerosols over the Amazon Basin during the Wet and Dry Seasons. *Atmos. Chem. Phys.* **2012**, *12*, 6041–6065. [CrossRef]
23. Huang, J.; Guo, J.; Wang, F.; Liu, Z.; Jeong, M.-J.; Yu, H.; Zhang, Z. CALIPSO Inferred Most Probable Heights of Global Dust and Smoke Layers. *J. Geophys. Res. Atmos.* **2015**, *120*, 5085–5100. [CrossRef]
24. Bourgeois, Q.; Ekman, A.M.L.; Krejci, R. Aerosol Transport over the Andes from the Amazon Basin to the Remote Pacific Ocean: A Multiyear CALIOP Assessment. *J. Geophys. Res. Atmos.* **2015**, *120*, 8411–8425. [CrossRef]

25. Marenco, F.; Johnson, B.; Langridge, J.M.; Mulcahy, J.; Benedetti, A.; Remy, S.; Jones, L.; Szpek, K.; Haywood, J.; Longo, K.; et al. On the Vertical Distribution of Smoke in the Amazonian Atmosphere during the Dry Season. *Atmos. Chem. Phys.* **2016**, *16*, 2155–2174. [CrossRef]
26. Gonzalez-Alonso, L.; Val Martin, M.; Kahn, R.A. Biomass-Burning Smoke Heights over the Amazon Observed from Space. *Atmos. Chem. Phys.* **2019**, *19*, 1685–1702. [CrossRef]
27. Koch, D.; Bond, T.C.; Streets, D.; Unger, N.; der Werf, G.R. Global Impacts of Aerosols from Particular Source Regions and Sectors. *J. Geophys. Res. Atmos.* **2007**, *112*, D02205. [CrossRef]
28. Romero-Ruiz, M.; Etter, A.; Sarmiento, A.; Tansey, K. Spatial and Temporal Variability of Fires in Relation to Ecosystems, Land Tenure and Rainfall in Savannas of Northern South America. *Glob. Chang. Biol.* **2010**, *16*, 2013–2023. [CrossRef]
29. Pereira, G.; Shimabukuro, Y.E.; Moraes, E.C.; Freitas, S.R.; Cardozo, F.S.; Longo, K.M. Monitoring the Transport of Biomass Burning Emission in South America. *Atmos. Pollut. Res.* **2011**, *2*, 247–254. [CrossRef]
30. Hamburger, T.; Matisāns, M.; Tunved, P.; Ström, J.; Calderon, S.; Hoffmann, P.; Hochschild, G.; Gross, J.; Schmeissner, T.; Wiedensohler, A.; et al. Long-Term in Situ Observations of Biomass Burning Aerosol at a High Altitude Station in Venezuela—Sources, Impacts and Interannual Variability. *Atmos. Chem. Phys.* **2013**, *13*, 9837–9853. [CrossRef]
31. Gonçalves, C.; Figueiredo, B.R.; Alves, C.A.; Cardoso, A.A.; da Silva, R.; Kanzawa, S.H.; Vicente, A.M. Chemical Characterisation of Total Suspended Particulate Matter from a Remote Area in Amazonia. *Atmos. Res.* **2016**, *182*, 102–113. [CrossRef]
32. Mendez-Espinosa, J.F.; Belalcazar, L.C.; Betancourt, R.M. Regional Air Quality Impact of Northern South America Biomass Burning Emissions. *Atmos. Environ.* **2019**, *203*, 131–140. [CrossRef]
33. Pérez-Ramírez, D.; Andrade-Flores, M.; Eck, T.F.; Stein, A.F.; O'Neill, N.T.; Lyamani, H.; Gassó, S.; Whiteman, D.N.; Veselovskii, I.; Velarde, F.; et al. Multi Year Aerosol Characterization in the Tropical Andes and in Adjacent Amazonia Using AERONET Measurements. *Atmos. Environ.* **2017**, *166*, 412–432. [CrossRef]
34. Ulke, A.G.; Freitas, S.R.; Longo, K.M. Aerosol Load and Characteristics in Buenos Aires: Relationships with Dispersion Mechanisms and Sources in South America. In *Proceedings of the Air Pollution Modeling and Its Application XXI*; Steyn, D.G., Trini Castelli, S., Eds.; Springer: Dordrecht, The Netherlands, 2012; pp. 251–255. [CrossRef]
35. Otero, L.A.; Ristori, P.R.; Holben, B.; Quel, E. Espesor óptico de aerosoles durante el año 2002 para diez estaciones pertenecientes a la Red AERONET NASA. *Óptica Pura Y Apl.* **2006**, *39*, 355–364.
36. Otero, L.A.; Ristori, P.R.; García Ferreyra, M.F.; Herrera, M.E.; Bali, J.L.; Pereyra, A.F.; Martorrella, E.; Brusca, S.; D'Elia, R.L.; Fierro, V.E.; et al. Siete Fotómetros de la Red AERONET instalados en Territorio Argentino: Análisis estadísticos de los datos y caracterización de los aerosoles. *Anales (Asoc. Física Argent.)* **2018**, *29*, 78–82. [CrossRef]
37. Casasola, F.; Pereyra, C.; Prieto, M.; Martonella, E.; Brusca, S.; Raponi, M.; Ristori, P.; Otero, L. Clasificación de Los Aerosoles En La Estación AERONET de Tucumán, Argentina. *Anales (Asoc. Física Argent.)* **2020**, *31*, 39–45. [CrossRef]
38. García, M.E.; Della Ceca, L.S.; Micheletti, M.I.; Piacentini, R.D.N.; Ordano, M.A.; Reyes, N.J.F.; Buedo, S.; González, J.A. Satellite and Ground Atmospheric Particulate Matter Detection over Tucumán City, Argentina, Space-Time Distribution, Climatic and Seasonal Variability. *AIMS Environ. Sci.* **2018**, *5*, 173–194. [CrossRef]
39. Della Ceca, L.S.; Ferreyra, M.F.G.; Lyapustin, A.; Chudnovsky, A.; Otero, L.; Carreras, H.; Barnaba, F. Satellite-Based View of the Aerosol Spatial and Temporal Variability in the Córdoba Region (Argentina) Using over Ten Years of High-Resolution Data. *ISPRS J. Photogramm. Remote Sens.* **2018**, *145*, 250–267. [CrossRef] [PubMed]
40. Olcese, L.E.; Palancar, G.G.; Toselli, B.M. Aerosol Optical Properties in Central Argentina. *J. Aerosol Sci.* **2014**, *68*, 25–37. [CrossRef]
41. Li, J.; Pósfai, M.; Hobbs, P.V.; Buseck, P.R. Individual Aerosol Particles from Biomass Burning in Southern Africa: 2, Compositions and Aging of Inorganic Particles. *J. Geophys. Res. Atmos.* **2003**, *108*, 2310. [CrossRef]
42. Eck, T.F.; Holben, B.N.; Reid, J.S.; Dubovik, O.; Smirnov, A.; O'neill, N.T.; Slutsker, I.; Kinne, S. Wavelength Dependence of the Optical Depth of Biomass Burning, Urban, and Desert Dust Aerosols. *J. Geophys. Res. Atmos.* **1999**, *104*, 31333–31349. [CrossRef]
43. Dubovik, O.; Holben, B.; Eck, T.F.; Smirnov, A.; Kaufman, Y.J.; King, M.D.; Tanré, D.; Slutsker, I. Variability of Absorption and Optical Properties of Key Aerosol Types Observed in Worldwide Locations. *J. Atmos. Sci.* **2002**, *59*, 590–608. [CrossRef]
44. Müller, D.; Ansmann, A.; Mattis, I.; Tesche, M.; Wandinger, U.; Althausen, D.; Pisani, G. Aerosol-Type-Dependent Lidar Ratios Observed with Raman Lidar. *J. Geophys. Res. Atmos.* **2007**, *112*, D16202. [CrossRef]
45. Nepomuceno Pereira, S.; Preißler, J.; Guerrero-Rascado, J.L.; Silva, A.M.; Wagner, F. Forest Fire Smoke Layers Observed in the Free Troposphere over Portugal with a Multiwavelength Raman Lidar: Optical and Microphysical Properties. *Sci. World J.* **2014**, *2014*, 421838. [CrossRef]
46. Reid, J.S.; Lagrosas, N.D.; Jonsson, H.H.; Reid, E.A.; Sessions, W.R.; Simpas, J.B.; Uy, S.N.; Boyd, T.J.; Atwood, S.A.; Blake, D.R.; et al. Observations of the Temporal Variability in Aerosol Properties and Their Relationships to Meteorology in the Summer Monsoonal South China Sea/East Sea: The Scale-Dependent Role of Monsoonal Flows, the Madden–Julian Oscillation, Tropical Cyclones, Squall. *Atmos. Chem. Phys.* **2015**, *15*, 1745–1768. [CrossRef]
47. Eck, T.F.; Holben, B.N.; Ward, D.E.; Mukelabai, M.M.; Dubovik, O.; Smirnov, A.; Schafer, J.S.; Hsu, N.C.; Piketh, S.J.; Queface, A.; et al. Variability of Biomass Burning Aerosol Optical Characteristics in Southern Africa during the SAFARI 2000 Dry Season Campaign and a Comparison of Single Scattering Albedo Estimates from Radiometric Measurements. *J. Geophys. Res. Atmos.* **2003**, *108*, D13. [CrossRef]

48. Dubovik, O.; Sinyuk, A.; Lapyonok, T.; Holben, B.N.; Mishchenko, M.; Yang, P.; Eck, T.F.; Volten, H.; Muñoz, O.; Veihelmann, B.; et al. Application of Spheroid Models to Account for Aerosol Particle Nonsphericity in Remote Sensing of Desert Dust. *J. Geophys. Res. Atmos.* **2006**, *111*, D11208. [CrossRef]
49. Karra, K.; Kontgis, C.; Statman-Weil, Z.; Mazzariello, J.C.; Mathis, M.M.; Brumby, S.P. Global Land Use/Land Cover with Sentinel 2 and Deep Learning. In Proceedings of the 2021 IEEE International Geoscience and Remote Sensing Symposium IGARSS 2021, Brussels, Belgium, 11–16 July 2021; pp. 4704–4707. [CrossRef]
50. Holben, B.N.; Slutsker, T.I.E.I.; Tar, D.; Buis, J.P.; Setxerj, I.I.A.; Reagan, A.; Kaufman, Y.J.; Nakajima, T.; Lavenu, F.; Vemte, E.; et al. AERONET-A Federated Instrument Network and Data Archive for Aerosol Characterization. *Remote Sens. Environ.* **1998**, *16*, 1–16. [CrossRef]
51. Smirnov, A.; Holben, B.N.; Eck, T.F.; Dubovik, O.; Slutsker, I. Cloud-Screening and Quality Control Algorithms for the AERONET Database. *Remote Sens. Environ.* **2000**, *73*, 337–349. [CrossRef]
52. Eck, T.F.; Holben, B.N.; Dubovik, O.; Smirnov, A.; Goloub, P.; Chen, H.B.; Chatenet, B.; Gomes, L.; Zhang, X.-Y.; Tsay, S.-C.; et al. Columnar Aerosol Optical Properties at AERONET Sites in Central Eastern Asia and Aerosol Transport to the Tropical Mid-Pacific. *J. Geophys. Res. Atmos.* **2005**, *110*, D06202. [CrossRef]
53. Boselli, A.; Caggiano, R.; Cornacchia, C.; Madonna, F.; Mona, L.; Macchiato, M.; Pappalardo, G.; Trippetta, S. Multi Year Sun-Photometer Measurements for Aerosol Characterization in a Central Mediterranean Site. *Atmos. Res.* **2012**, *104*, 98–110. [CrossRef]
54. Papandrea, S. Red SAVER-Net: Descripción General, Instrumental Involucrado y Productos Generados, Technical Note on National Meteorological Service of Argentina 2020-70. Available online: http://repositorio.smn.gob.ar/handle/20.500.12160/1362 (accessed on 5 February 2023).
55. Papandrea, S.; Pallotta, J.V. Introducción Al Procesamiento de Señales Lidar: Telemetría de Nubes y Altura de Capa Límite Atmosférica, Technical Note on National Meteorological Service of Argentina 2020-73. Available online: http://repositorio.smn.gob.ar/handle/20.500.12160/1375 (accessed on 5 February 2023).
56. Fernald, F.G. Analysis of Atmospheric Lidar Observations: Some Comments. *Appl. Opt.* **1984**, *23*, 652–653. [CrossRef]
57. Shimizu, A.; Nishizawa, T.; Jin, Y.; Kim, S.-W.; Wang, Z.; Batdorj, D.; Sugimoto, N. Evolution of a Lidar Network for Tropospheric Aerosol Detection in East Asia. *Opt. Eng.* **2017**, *56*, 31219. [CrossRef]
58. Veefkind, J.P.; Aben, I.; McMullan, K.; Förster, H.; de Vries, J.; Otter, G.; Claas, J.; Eskes, H.J.; de Haan, J.F.; Kleipool, Q.; et al. TROPOMI on the ESA Sentinel-5 Precursor: A GMES Mission for Global Observations of the Atmospheric Composition for Climate, Air Quality and Ozone Layer Applications. *Remote Sens. Environ.* **2012**, *120*, 70–83. [CrossRef]
59. Giglio, L.; Schroeder, W.; Justice, C.O. The Collection 6 MODIS Active Fire Detection Algorithm and Fire Products. *Remote Sens. Environ.* **2016**, *178*, 31–41. [CrossRef] [PubMed]
60. Winker, D.M.; Pelon, J.; Coakley, J.A.; Ackerman, S.A.; Charlson, R.J.; Colarco, P.R.; Flamant, P.; Fu, Q.; Hoff, R.M.; Kittaka, C.; et al. The CALIPSO Mission: A Global 3D View of Aerosols and Clouds. *Bull. Am. Meteorol. Soc.* **2010**, *91*, 1211–1230. [CrossRef]
61. Draxler, R.R.; Rolph, G.D. Evaluation of the Transfer Coefficient Matrix (TCM) Approach to Model the Atmospheric Radionuclide Air Concentrations from Fukushima. *J. Geophys. Res. Atmos.* **2012**, *117*, 1–10. [CrossRef]
62. Draxler, R.R. Evaluation of an Ensemble Dispersion Calculation. *J. Appl. Meteorol. Climatol.* **2003**, *42*, 308–317. [CrossRef]
63. Stein, A.F.; Draxler, R.R.; Rolph, G.D.; Stunder, B.J.B.; Cohen, M.D.; Ngan, F. NOAA's HYSPLIT Atmospheric Transport and Dispersion Modeling System. *Bull. Am. Meteorol. Soc.* **2015**, *96*, 2059–2077. [CrossRef]
64. Adam, M.; Fragkos, K.; Solomos, S.; Belegante, L.; Andrei, S.; Talianu, C.; Mărmureanu, L.; Antonescu, B.; Ene, D.; Nicolae, V.; et al. Methodology for Lidar Monitoring of Biomass Burning Smoke in Connection with the Land Cover. *Remote Sens.* **2022**, *14*, 4734. [CrossRef]